AFRL-AFOSR-VA-TR-2019-0190

Diode Pumped Rare-gas Lasers

Michael Heaven
EMORY UNIVERSITY

08/29/2017
Final Report

DISTRIBUTION A: Distribution approved for public release.

Air Force Research Laboratory
AF Office Of Scientific Research (AFOSR)/ RTB1
Arlington, Virginia 22203
Air Force Materiel Command

REPORT DOCUMENTATION PAGE

Form Approved
OMB No. 0704-0188

The public reporting burden for this collection of information is estimated to average 1 hour per response, including the time for reviewing instructions, searching existing data sources, gathering and maintaining the data needed, and completing and reviewing the collection of information. Send comments regarding this burden estimate or any other aspect of this collection of information, including suggestions for reducing the burden, to Department of Defense, Washington Headquarters Services, Directorate for Information Operations and Reports (0704-0188), 1215 Jefferson Davis Highway, Suite 1204, Arlington, VA 22202-4302. Respondents should be aware that notwithstanding any other provision of law, no person shall be subject to any penalty for failing to comply with a collection of information if it does not display a currently valid OMB control number.
PLEASE DO NOT RETURN YOUR FORM TO THE ABOVE ADDRESS.

1. REPORT DATE *(DD-MM-YYYY)*	2. REPORT TYPE	3. DATES COVERED *(From - To)*
08/25/2017	Final	11/01/2012-08/25/2017

4. TITLE AND SUBTITLE
Diode Pumped Rare Gas Lasers

5a. CONTRACT NUMBER
FA9550-13-1-0002

5b. GRANT NUMBER

5c. PROGRAM ELEMENT NUMBER

6. AUTHOR(S)
Michael C. Heaven, W. Terry Rawlings and Glen P. Perram

5d. PROJECT NUMBER

5e. TASK NUMBER

5f. WORK UNIT NUMBER

7. PERFORMING ORGANIZATION NAME(S) AND ADDRESS(ES)
Emory University, Department of Chemistry, 1515 Dickey Drive, Atlanta GA 30322
Physical Sciences Inc., 20 New England Business Center Andover, MA 01810
Department of Engineering Physics, AFIT, Dayton, OH 45433

8. PERFORMING ORGANIZATION REPORT NUMBER

9. SPONSORING/MONITORING AGENCY NAME(S) AND ADDRESS(ES)
AFOSR
875 N. Randolph St.
Suite 325, Rm 3112
Arlington, VA 22203

10. SPONSOR/MONITOR'S ACRONYM(S)

11. SPONSOR/MONITOR'S REPORT NUMBER(S)

12. DISTRIBUTION/AVAILABILITY STATEMENT
DISTRIBUTION A: Distribution approved for public release.

13. SUPPLEMENTARY NOTES

14. ABSTRACT
Continuous wave optically pumped Ar* lasers were demonstrated using discharges driven by strip resonator micro-arrays or bare metal electrodes powered by short duration, high voltage pulse trains. The micro-array laser exhibited an optical-to-optical power conversion efficiency of 55% at a total output power of 40 mW. The larger volume pulsed discharge system produced 4.1 W of output power with an optical conversion efficiency of 31%. These results were used to validate computational models that predict scaling into the kW range and beyond is feasible for the Ar*/He lasing medium. Pulsed laser demonstrations have been performed with Kr*/He and Xe*/He gas mixtures. Both show promise for scaling.

15. SUBJECT TERMS
High-power lasers, hybrid solid state / gas phase lasers, wavelength agility, high beam quality system.

16. SECURITY CLASSIFICATION OF:			17. LIMITATION OF ABSTRACT	18. NUMBER OF PAGES	19a. NAME OF RESPONSIBLE PERSON
a. REPORT	b. ABSTRACT	c. THIS PAGE			Michael C. Heaven
unclassified	unclassified	unclassified	none		19b. TELEPHONE NUMBER *(Include area code)* 404 727 6617

Diode Pumped Rare Gas Lasers

High Energy Laser Joint Technology Office
Multi-Disciplinary Research Initiative

Grant FA9550-13-1-0002

Final Report
August 23, 2017

Lead Principal Investigator:

Michael Heaven
Department of Chemistry
Emory University
Atlanta, GA 30322

Co-Principal Investigators:

Glen P. Perram
Department of Engineering Physics
Air Force Institute of Technology
Wright-Patterson Air Force Base, OH 45433-7765

Steven J. Davis, W. Terry Rawlins and Kristin L. Galbally-Kinney
Physical Sciences Inc.
20 New England Business Center
Andover, MA 01810

A. R. Hoskinson and J. A. Hopwood
Electrical and Computer Engineering Department
Tufts University
Medford, MA USA 02155

Abstract

Diode-pumped rare gas lasers show promise for the construction of efficient high-power lasers that have high beam quality and long-range propagation characteristics. This program has focused on the development of the optically pumped rare gas laser concept through laser demonstration experiments, innovations in high-pressure gas discharges and computational modeling. Measurements of energy transfer rate constants and pressure broadening coefficients were made to provide key modeling parameters.

It was established that the gas discharge must provide rare gas metastable densities in excess of 10^{12} cm^{-3} to sustain efficient lasing. Continuous wave optically pumped Ar* lasers were demonstrated using discharges driven by strip resonator micro-arrays or bare metal electrodes powered by short duration, high voltage pulse trains. The micro-array laser exhibited an optical-to-optical power conversion efficiency of 55% at a total output power of 40 mW. The larger volume pulsed discharge system produced 4.1 W of output power with an optical conversion efficiency of 31%. These results were used to validate computational models that predict scaling into the kW range and beyond is feasible for the Ar*/He lasing medium. Studies of alternative high-pressure discharge configurations were also carried out. These included dielectric barrier, micro hollow cathode array and capacitively coupled RF discharges. High yields of Ar* metastables were achieved with the two former techniques.

Pulsed laser demonstrations have been performed with Kr*/He and Xe*/He gas mixtures. These systems show promise and are worthy of further investigation.

Publications supported by grant FA9550-13-1-0002

J. Han, L. Glebov, G. Venus, and M. C. Heaven, Opt. Lett. **38**, 5458 (2013)
"Demonstration of a diode-pumped metastable Ar laser"
J. Han and M. C. Heaven, Opt. Lett. **39**, 6541 (2014)
"Kinetics of optically-pumped Ar metastables"
W. T. Rawlins, K. L. Galbally-Kinney, S. J. Davis, A. R. Hoskinson, J. A. Hopwood, and M. C. Heaven, Optics Express, **23**, 4804 (2015)
"Optically pumped microplasma rare gas laser"
J. Han, M.C. Heaven, Opt. Lett., **40,** 1310-1313 (2015)
"Kinetics of optically pumped Kr metastables"
V. N. Azyazov, A. P. Torbin, A. M. Mebel, S. Bresler, M. C. Heaven, Proc. SPIE 9729, High Energy/Average Power Lasers and Intense Beam Applications IX, 972909 (2016); doi:10.1117/12.2218119
"Deactivation and reaction of excited states of Rb in collisions with H_2, CH_4 and C_2H_6"
P. A. Mikheyev, A. K. Churnyshov, N. I. Ufimtsev, A. R. Ghildina, V. N. Azyazov, M. C. Heaven, Proc. SPIE 9729, High Energy/Average Power Lasers and Intense Beam Applications IX, 97290E (2016); doi:10.1117/12.2218349
"Measurement of pressure broadening of the Kr 811.3 nm absorption line using a diode laser"
J. Han, M. C. Heaven, D. Emmons, G. P. Perram, D. E. Weeks, W. F. Bailey, Proc. SPIE 9729, High Energy/Average Power Lasers and Intense Beam Applications IX, 97290D (2016); doi:10.1117/12.2218122
"Pulsed discharge production Ar metastables"*
V. N. Azyazov, S. M. Bresler, A. P. Torbin, A. M. Mebel, and M. C. Heaven, Opt. Lett., **41**, 669 (2016)
"Removal of Rb(6P) by H_2, CH_4 and C_2H_6"
V. N. Azyazov, A. P. Torbin, A. M. Mebel, S. M. Brawler and M. C. Heaven, J. Quant. Spectrosc. Rad. Trans., **196**, 46-52 (2017)
"Product channels of the reactions of Rb(6^2P) with H_2, CH_4 and C_2H_6"
J. Han, M. C. Heaven, P. J. Moran, G. A. Pitz, E. M. Guild, C. R. Sanderson, and B. Hokr, J. Directed Energy **6**, 209 - 219 (2017).
"Pulsed discharge – diode pumped Ar laser"*
A. R. Hoskinson, J. Gregório, J. Hopwood, K. L. Galbally-Kinney, S. J. Davis, and W. T. Rawlins, J. Appl. Phys., **121**, 153302 (2017)
"Spatially resolved modeling and measurements of metastable argon atoms in argon-helium microplasmas,"
A. R. Hoskinson, J. Gregório, J. Hopwood, K. Galbally-Kinney, S. J. Davis, and W. T. Rawlins, J. Appl. Phys., **119**, 233301 (2016)
"Argon metastable production in argon-helium microplasmas,"
B. Eshel, C. A. Rice, and G. P. Perram, J. Quant. Spectros. Rad. Trans. **179**, 40-50 (2016).
"Pressure broadening and shift rates for Ar (s-p) transitions observed in an Ar-He discharge"
Ben Eshel, AFIT MS Thesis, AFIT-ENP-13-J-02D, June 2013
"Spectral Analysis and Metastable Absorption Measurements of High Pressure, Capacitively and Inductively Coupled Radio-Frequency Argon-Helium Discharges",

Manuscripts in preparation/in review

Daniel J. Emmons, David E. Weeks, Ben Eshel, and Glen P. Perram, Submitted Aug 2017.
"Metastable Ar($1s_5$) Density Dependence on Pressure and Argon-Helium Composition in a High Pressure Radio Frequency Dielectric Barrier Discharge",
Ben Eshel and Glen P. Perram, to be submitted to J Optical Society of America B, Aug 2017.
"A five-level Ar-He laser model for characterization of a diode-pumped rare gas laser"
Ben Eshel, Steven Owens, Christopher A. Rice, and Glen P. Perram, submitted to Optics Commun., July 2017.
"Saturation spectroscopy of an optically opaque argon plasma"

Introduction

Hybrid gas phase / solid state lasers show promise for the construction of efficient high-power lasers that have high beam quality and long-range propagation characteristics. The best-known example is the diode-pumped alkali vapor laser (DPAL), which is now developed to the point of being a kW class device [1-5]. The outlook for scaling DPAL systems to 100 kW class devices in the near term remains promising. However, there are a number of engineering challenges. One set of problems stem from the chemically aggressive nature of the alkali metal vapors. In the presence of an intense light field, these reactants destroy the inner surfaces of the gain cell windows. Other unwanted reactions can include the buffer gas used to induce spin-orbit relaxation between the ^{2}P levels. In a typical DPAL, He buffer gas is used to pressure broaden the absorption lines to improve the spectral overlap with the pump laser radiation. However, helium and the other rare-gases have low cross sections for spin-orbit relaxation of the heavier alkali metals. If He alone is used for spin-orbit relaxation, this necessitates the use of very high gas pressures that will degrade the beam quality of the laser. The solution has been to add a second buffer gas component that induces rapid spin-orbit relaxation, without significantly quenching the ^{2}P levels. Small hydrocarbons such as methane and ethane have proven to be effective. The downside of using these reagents is that they react with the alkali metals to produce hydrides ("laser snow") and carbonaceous deposits (particularly on the windows, where the reactions are facilitated by photoexcitation) [6].

There is interest in developing DPAL analog systems in order to circumvent the chemical problems and expand the range of pump and lasing wavelength that can be employed. Unfortunately, there are few alternate systems when limiting the search to atoms that can be optically pumped from the ground state. During the past few years we have explored the idea of optically pumping atoms that are in metastable electronic states. It is well known that rare gas atoms (Rg=Ne, Ar, Kr, Xe), excited to the metastable $np^5(n+1)s\ ^3P_2$ states, have spectroscopic properties that are closely similar to those of the alkali atoms [7]. These metastables (indicated by Rg* in the following) can be generated using low power electrical discharges. Lasing of the metastable atoms is achieved by optical pumping of the $np^5(n+1)p \leftarrow np^5(n+1)s$ transitions [8-12]. As an example, the relevant energy levels of Ar* are shown in Fig. 1, where they are labeled using both labeled using both Racah and Paschen notations. There are four levels ($1s_5$, $1s_4$, $1s_3$ and $1s_2$) associated with the $np^5(n+1)s$ configuration, and ten levels ($2p_1$-$2p_{10}$) that arise from $np^5(n+1)p$. In Paschen notation the energies decrease as the subscripted index increases. Lasing is achieved by pumping the $2p_9 \leftarrow 1s_5$ transition and lasing on $2p_{10} \rightarrow 1s_5$. The energy transfer step needed to create a population inversion can be accomplished using He as the collision partner [13, 14]. Hence, the entire lasing medium is chemically inert. The primary technical challenge for the Rg* laser is the requirement that a metastable number density in excess of 10^{12} cm^{-3} must be generated in the presence of 0.5 – 1 atm of He.

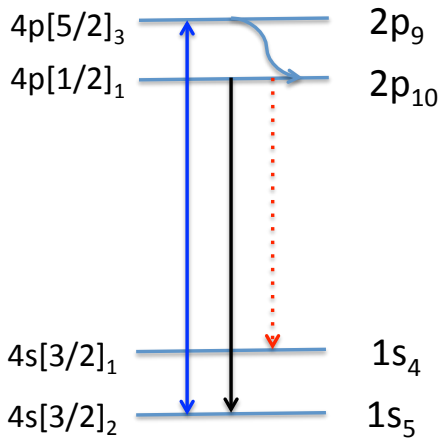

Figure 1. Energy levels of Ar* involved in the optically pumped laser.

Section 1: Studies of optically pumped Rg* lasers and Rg* collisional energy transfer at Emory University

The group at Emory University (EU) studied pulsed discharges and dielectric barrier discharges as methods to generate [Rg*]>10^{12} cm^{-3} in the presence of Helium at pressures in excess of 0.5 atm. They also examined Rg* collisional energy transfer kinetics as a function of temperature. The latter studies were carried out to facilitate modeling of diode pumped Rg* laser systems.

Reference [9] describes an Ar*/He laser that was pumped by a line-narrowed diode laser. The Ar* metastables were produced in a parallel plate discharge that was driven by voltage pulses of 1000-2000 V, with a pulse duration of 1 μs and repetition frequency of 1kHz. The apparatus used for these experiments is shown in Fig. 2.

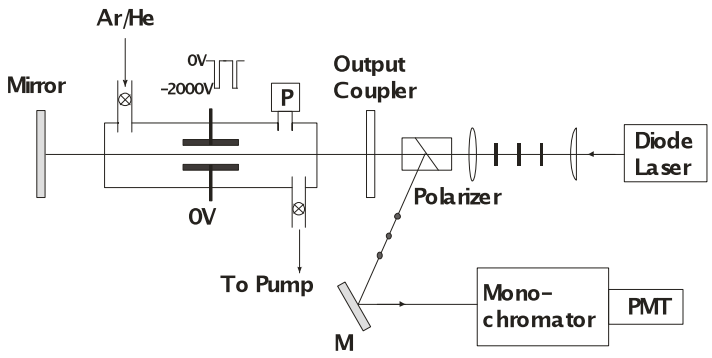

Fig.2 . Experimental setup for an Ar* laser with a CW diode pump source.

Optical absorption measurements indicated that reasonably high Ar* number densities were being generated, and that the lifetime was on the order of 7 μs. However, the lasing typically exhibited pulse durations in the range of 100-200 ns. Diagnostic measurements indicated that Ar* metastables were only produced at the beginning of each discharge pulse (when the electric field / number density (E/N) ratio is high), and that optical pumping was transferring population to the $1s_4$ level. The loss of population from $1s_5$ was responsible for the termination of the laser pulse.

CW lasing with 55% photon conversion efficiency was initially demonstrated by the PSI group using a high-frequency micro-discharge to generate Ar($1s_5$) ([10], see below). The challenge for the micro-discharge, with respect to power scaling, was that only a small volume of gas could be excited using the prototype discharge array. Methods for increasing the volume are being pursued by the groups at PSI and Tufts University.

At Emory, the focus has been on the development of larger scale discharge configurations that utilize relatively short duration high voltage pulses to generate Ar*. As the lifetime of Ar* is on the order of several tens of microseconds under the conditions used, pulse repetition rates in excess of 100 kHz produced good steady state populations of Ar*. This approach was guided by the computational model of pulsed Ar* production that was developed by Emmons et al.[15] Fig. 3 shows the apparatus used for this second series of pulsed discharge experiments.

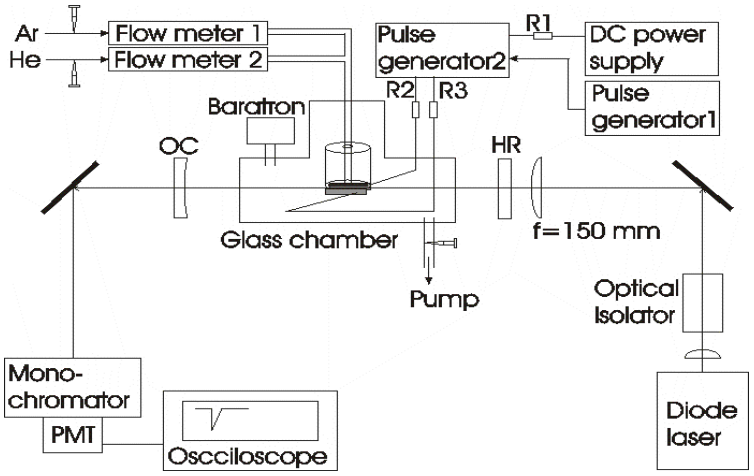

Fig. 3. Schematic of the equipment used for optically pumped lasing of Ar* on the $2p_{10} \rightarrow 1s_5$ transition.

A T-shaped Pyrex glass cell (50 mm outer diameter) was used for gas handling. Ultra-high purity Ar and He gases were introduced into the cell from a side arm. Metering valves on the gas input lines and a choke valve on the vacuum pump were used to control the gas flow rates and total pressure in the cell. Two mass-flow meters and a capacitance manometer were used to determine the partial pressures of Ar and He. Inside the cell the end of the gas delivery line was positioned on the edge of the gap between the parallel plate electrodes. The end of the tube was configured to deliver the gas through a rectangular slot that was 1 mm wide and 20 mm long. The flow rates used in these experiments were low, typically of the order of 1.7 L/minute for total pressures in the range 400-500 Torr. The stainless steel electrodes were made from 20 mm long bars that had a square cross section of 6 mm x 6 mm. The spacing between the electrodes was 3 mm. The gas cell was mounted on an x-y translation stage, to permit optimization of the discharge zone relative to the pump laser beam. A variable DC power supply (with a maximum rating of 500V/125 mA) was used to charge the internal capacitor of a high voltage pulse generator (DEI PVX-4140) through a 5 kΩ current-limiting resistor. A low voltage pulse generator (Quantum Composers, 9600) was used to define the pulse-width and repetition rate of the output from the high voltage pulse generator. The high voltage output was connected to the stainless steel electrodes. To protect the output stage of the high voltage pulse generator, a 500 Ω resistor was used to limit the discharge current. The transient discharge current was monitored using the voltage drop across a small resistor (R_3 = 0.5Ω) inserted in the path to ground. The transient voltage was recorded with a digital oscilloscope (LeCroy,WaveSurfer 24Xs), connected via a 1000:1 voltage divider. Note that the voltage divider was an integral component of the high voltage pulse generator.

The discharge cell was positioned inside an optical cavity, as shown in Fig. 3. Dichroic mirrors were used to permit longitudinal optical pumping of the gas discharge. The high reflecting mirror (HR) was coated for minimal reflection (<0.1%) at the pumping wavelength (811. 5 nm) and 100% reflection for the lasing wavelength (912.3 nm). The output coupler (OC) was coated for 100% reflection at the pump wavelength, and 95% reflection for the lasing wavelength. The OC had a radius of curvature of 2 m. The distance between the OC and HR was 350 mm. The windows on the glass chamber were both uncoated fused silica optical flats.

A commercial tunable diode laser (OptiGrate, 30 W Shark Laser System) was used to optically pump the Ar $2p_9 \leftarrow 1s_5$ transition. This laser was provided on loan from the Air Force Research Laboratory (Kirtland AFB). Based on the manufacturers specifications, the laser had a

linewidth of 0.035 nm at 811.5 nm, when powered by a current of 50 A. Temperature controls for both the diode and the volume Bragg grating were used for wavelength tuning. The diode laser beam was transmitted through a polarization-maintaining fiber optic rod that had a core diameter of 600μm. The resulting output had a relatively large divergence angle. A 150 mm focal length convex lens was used to focus the pump beam at the center of the 20 mm long discharge zone. The diameter of the beam waist was about 1.6 mm at the center and about 2 mm at ends of the electrodes. The total power from the diode laser was measured just before the high reflector using a beam splitter and neutral density filters to reduce the power to a level that was within range for the available power meter (Ophir model 3A-P). The output from the Ar* laser was analyzed by means of a 0.25 M monochromator (Jarrell Ash 82-410) that was equipped with a Peltier-cooled photomultiplier (Hamamatsu, R1797). Measurements of the Ar* column densities were made using tunable diode laser absorption spectroscopy (TDLAS). Integration of the area encompassed by the absorption line was used to avoid the complications (and uncertainties) of line-shape analyses.

The discharge behavior depended on many factors, including gas composition, total pressure, flow rate, applied voltage, pulse duration and pulse repetition frequency. Initially, the conditions that produced uniform glow discharges were determined using visual observations. Low pressures, short pulse durations and low repetition frequencies favored discharges that completely filled the space between the electrodes. However, these conditions did not yield the best laser performance. The most intense lasing was obtained under conditions that caused the discharge to contract into a single filament, with a diameter that was dependent on the specific conditions. For the results reported here, the diameter of the filament was judged to be in the 1 – 2 mm range.

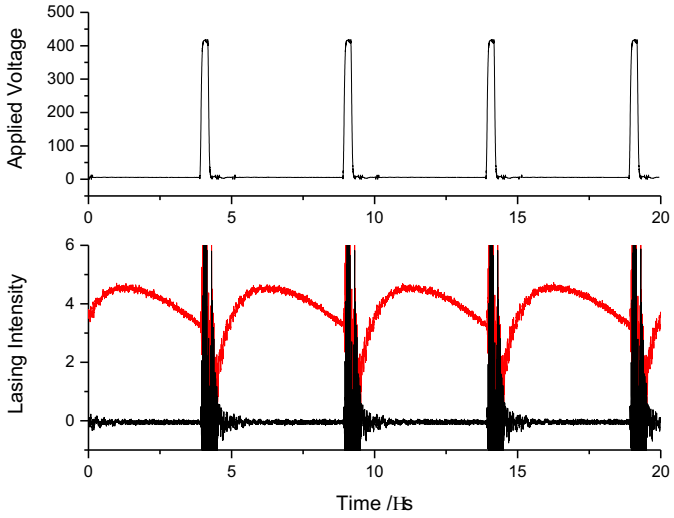

Fig. 4. Time-dependent traces for the voltage applied to the discharge electrodes (upper panel) and the lasing output (lower panel). The vertical axis of the lower panel shows the uncalibrated response of the detector to the laser light selected by the monochromator. The lowest trace, which shows only rf noise, was recorded with the OC misaligned.

Lasing was confirmed by checking the dependence on the discharge, pump wavelength, and sensitivity to the cavity alignment. The monochromator was used to verify single-line lasing

on the $2p_{10} \rightarrow 1s_5$ transition, and the laser output was easily observed using an IR sensitive phosphor card. Fig. 4 shows an example of the laser output for a discharge in 400 Torr of a 5% mixture of Ar in He. The upper panel shows the train of applied voltage pulses. The amplitude was 400V with a pulse duration of 0.3 μs and a repetition frequency of 200 kHz. The lower panel shows the output with the OC aligned (upper trace) and misaligned (lower trace). Note that the rapidly oscillating signals that are synchronous with the voltage pulses were due to radio frequency (rf) interference. The temporal behavior of the Ar* $1s_5$ metastables in this system was dramatically different to that observed in the first version of our pulsed discharge / CW optical pumping experiments [9]. Lasing was observed for the full 5 μs between discharge pulses, and there was a dip in the output power during the discharge pulse.

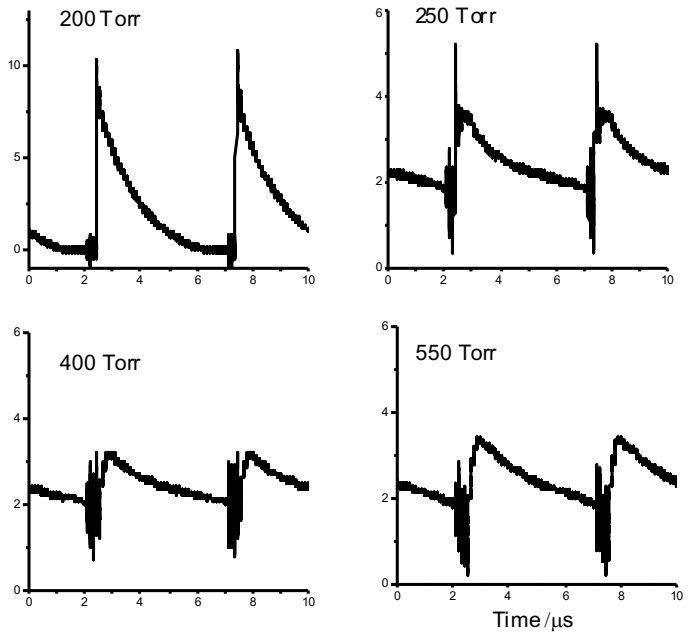

Fig. 5. Lasing output as a function of total gas pressure for 6%Ar in He. The vertical axes show the uncalibrated response of the detector to the laser light selected by the monochromator. The amplitudes are directly comparable to the vertical scale of the lower panel of Fig. 4.

Figure 5 shows the dependence of the lasing on the total gas pressure. These measurements were made using a gas mixture of 6% Ar in He. The voltage pulses were 400 V, 0.3 μs duration with a repetition frequency of 200 kHz. At 200 Torr the lasing output terminated before the next discharge pulse arrived. When the pressure was increased to 250 Torr the lasing was sustained between discharge pulses, resulting in modulated CW lasing. Further increase in the pressure, up to 400 Torr, produced an increase in the average output power. The discharge was not stable above 550 Torr. Fig. 6 shows the effect of changing the duration of the voltage pulse. Here it can be seen that increasing the duration beyond 0.3 μs results in a reduction in the laser output during the pulse. With a duration of 0.5 μs the lasing was briefly interrupted. At 0.8 μs the discharge became very bright and the lasing was completely suppressed.

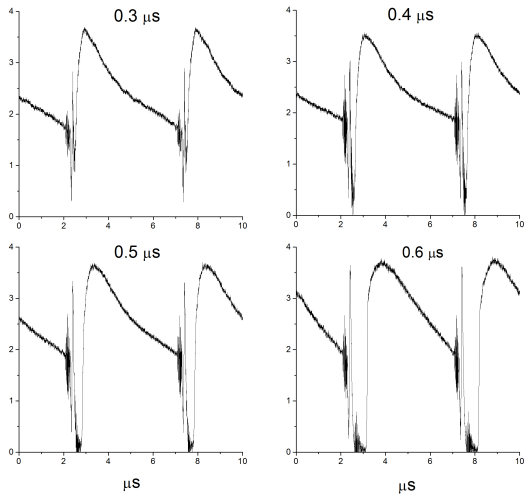

Fig. 6. Dependence of the laser output on the voltage pulse duration. Data for 5%Ar in He at 400 Torr. The vertical axes show the uncalibrated response of the detector to the laser light selected by the monochromator. The amplitudes are directly comparable to the vertical scale of the lower panel of Fig. 4.

The best performance was obtained for a 5% Ar /He mixture (400 Torr), with a 400 V, 0.3 μs, 200 kHz pulse train. These conditions produced a single discharge filament that was approximately 1.5 mm in diameter. The laser produced an average output power of 52 mW in a beam that exhibited a near TEM_{00} transverse mode quality. Note that the volume of the filament was less than the cavity mode volume. In a DPAL system this would significantly degrade performance, due to optical loss. However, the filament discharge likely exhibits little metastable density outside the filament, so the absorption loss would not be as great. To assess the divergence the beam was examined at a distance of 4.8 m from the output coupler. At this distance the diameter of the lasing spot was about 6 ~ 7 mm, in agreement with the theoretical value (6.4 mm) for the optical cavity.

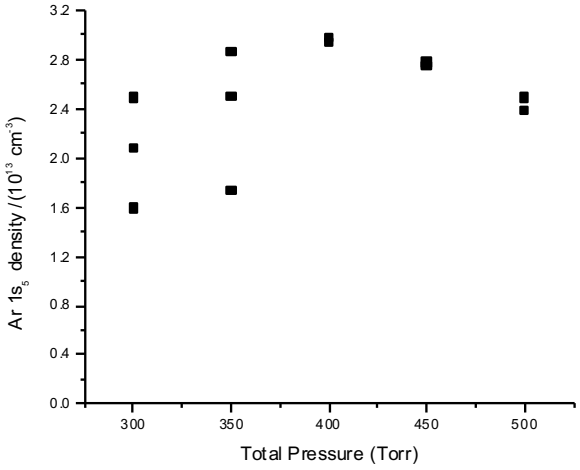

Fig. 7 Ar* $1s_5$ number density measurements for the single filament discharge. These data were recorded for a mixture of 5% Ar in He. The discharge pulses were 400V, for 0.3μs duration at 200 kHz.

Tunable diode laser absorption spectroscopy (TDLAS) of the $2p_{10}$-$1s_5$ transition was used to determine the Ar* $1s_5$ number densities in the filament discharges. Fig. 7 shows the number density as a function of the total gas pressure. Note that there were day-to-day fluctuations in the operation of the discharge, and the presence of multiple data points at a given pressure reflects this variability. We found that the most stable operation for this discharge mode was in the 400 to 450 Torr range, where the $1s_5$ number densities were approximately 2.6×10^{13} cm^{-3}.

Parametric studies of the pulsed discharge indicated that a larger discharge volume could be generated using higher voltage pulses of shorter durations. We subsequently obtained a larger power supply that permitted generation of 2000 V pulses of 80 ns duration at 200 kHz. A new gas cell was constructed for these experiments. The discharge electrodes were housed in a small chamber constructed from an Aluminum block with dimensions of 8.8x8.8x8.3 cm^3, bored through with 4, 4, and 6.3 cm diameter holes along three perpendicular axes. Each face was equipped with flanges or windows, and the system was evacuated to an ultimate vacuum of 10^{-2} Torr. Ultra-high purity Ar and He gases were continuously supplied to the chamber. Metering valves on the gas input lines and a choke valve on the vacuum pump were used to control the gas flow rates and total pressure in the chamber. Two mass-flow meters and a capacitance manometer were used to determine the partial pressures of Ar and He. Typically, the Ar:He ratio was 5.5:100, and the He mass flow rate was 5.2 L/min to sustain total pressures between 450 ~ 750 Torr. A pair of parallel, flat-face electrodes was mounted in the center of the chamber. The electrodes were cut from a stainless steel bar that had a square cross-section of 0.63x0.63 cm^2. Electrodes of length 1.5, 2.0, 2.5 or 3.0 cm were examined and had a typical spacing between the electrodes of 0.26 cm.

The discharge was operated in a repetitively pulsed mode. Typical discharge voltages were in the range of 1000 to 1500V, with the upper limit being constrained by the maximum current that could be tolerated by the high voltage pulse generator. The voltage pulses were of 80 ns duration, with a pulse repetition frequency of 200 kHz. Fig. 8 shows the discharge operating at 1000 V in 400 Torr of Ar (5%) in He. Here it can be seen that the discharge filled the entire volume between the electrodes.

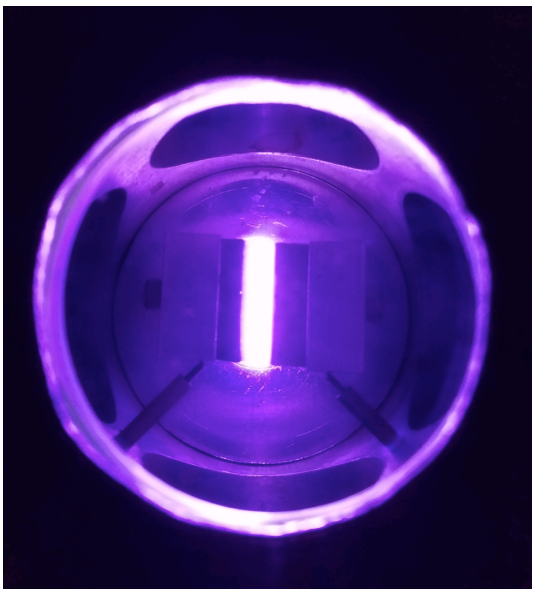

Fig. 8. Pulsed discharge in 400 Torr of Ar (5%) in He.

Metastable Ar* $1s_5$ densities were checked by means of TDLAS measurements. A time-averaged number density of 1.4×10^{13} cm^{-3} was achieved for the discharge shown in Fig. 8. Once the power from the diode laser was above threshold, Ar* lasing was easily realized. Experimental conditions were optimized in order to achieve the highest lasing power with the maximum pump power. Parameters that were varied included the percentage of Ar in the mixture, total pressure, mass flow rate, discharge voltage, repetition rate, output coupler (OC) reflectivity, focusing of the pump beam, electrode length and electrode gap. In the best case, 4.1 W of lasing from Ar* was realized with a 40% reflective OC, 720 Torr of a 5.3% Ar/He mixture, and a He flow rate of ~5L/min. The discharge was powered by 1500 V, 80 ns duration pulses at a repetition frequency of 200 kHz. The electrodes were 3.0 cm long, with a gap of 0.26 cm, and the fraction of the output power from the pump laser that overlapped the absorption line was 21 W. Ar* lasing was confirmed by checking the dependence on the discharge, pump wavelength, and sensitivity to the cavity alignment. Single-line lasing on the $2p_{10} \rightarrow 1s_5$ transition was verified using a monochromator.

Fig. 9 shows an example of the time-resolved laser output for a discharge in 710 Torr of a 5.3% mixture of Ar in He. In this case, an OC with 60% reflection was used and the electrodes were 2.5 cm long. The upper panel shows the train of applied voltage pulses, of amplitude 1300 V, pulse duration 80 ns and a repetition frequency of 200 kHz. The lower panel shows the lasing output at 912.3 nm (observed through the monochromator). This trace was generated by the subtraction of two signals – one from the lasing and a background trace recorded when the pump laser was blocked. This significantly reduced the electrical noise due to the discharge, but some residual radio frequency interference was present due to the imperfect subtraction. The most import observation was that, even with the very short discharge pulses, robust lasing persisted during the time between discharge pulses. An average output power of 3.4 W was obtained. Visual inspection of the beam, using a lens to expand the diameter to about 2 cm, indicated a high-quality transverse mode structure.

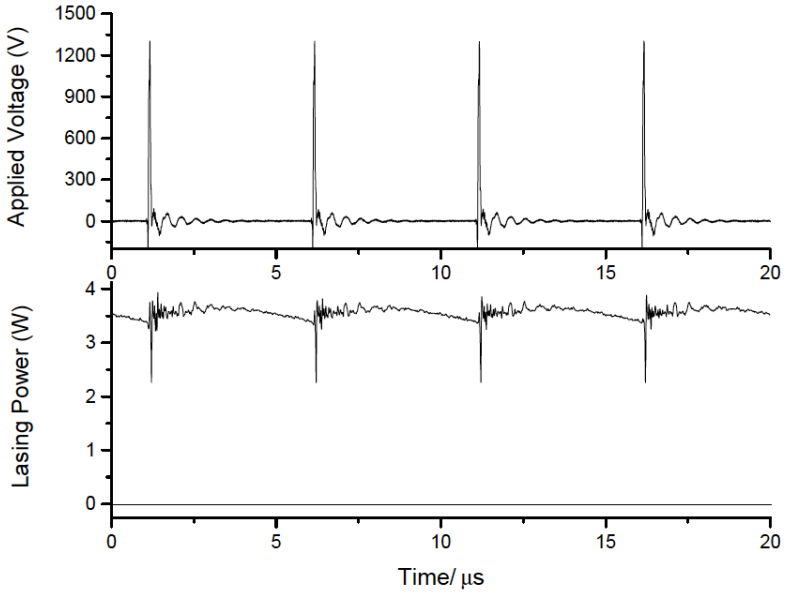

Fig. 9. Time-dependent traces for the voltage applied to the discharge electrodes (upper panel) and the lasing output (lower panel). The rapid oscillations are due to RF noise.

The optical-to-optical power conversion efficiency of the laser was 31%. It is established that higher efficiencies can be obtained with improvement of the spatial cavity mode overlap. An optical power conversion efficiency of 55% was demonstrated by Rawlins et al.[10], who used a Ti/Sapphire pump laser that had a high-quality transverse mode structure. Computational modeling indicates that the conversion efficiency can reach to 60-70% [16-18]. The present results constitute a significant step forward in the power scaling of the Ar* laser. The key improvement has been the development of a discharge that produces Ar* metastable densities $>10^{13}$ cm^3 in a volume of 0.5 cm^3. Metastable production steadily increased as the discharge voltage was increased. The best laser performance observed in this study was at the limit of voltage and the minimum pulse duration that could be obtained with the available equipment. We anticipate that further improvements in metastable production can be achieved with shorter duration, higher voltage pulses. The performance characteristics of the Ar* laser were consistent with published theoretical models [10, 16-19] and close to those of a typical DPAL system, indicating that scaling to >kW powers will be feasible.

Evaluation of dielectric barrier discharges for Ar* and Xe* production

The primary reason for difficulties in continuous metastable production at an atmospheric pressure is the low value of the reduced electric field E/N that occurs in continuous rare gas discharges. That leads to a low density of the energetic electrons needed for excitation of metastables, making atmospheric pressure continuous discharges inefficient for their production. Recent modeling of the Ar:He optically pumped rare gas laser (OPRGL)[17] had shown that efficient Ar($1s_5$) production is possible in discharges with E/N≈10 Td and larger. Extensive modeling performed in ref. [15] revealed that, even in a 20 μs pulsed discharge with bare electrodes in a 7% Ar in He mixture at 270 Torr, E/N values in the positive column right after the beginning of the discharge pulse became as low as 4-5 Td and were insufficient for efficient Ar($1s_5$) production. However, there are indications in the literature [20] that E/N≈7.5 Td might occur in the "positive column" of an atmospheric pressure dielectric barrier discharge (DBD) in He. Therefore, a DBD that is powered by an alternating voltage in the kilohertz range may be a possible solution for a quasi-continuous OPRGL.

The efficiency of the pump to lasing energy conversion strongly depends on collisional energy transfer paths in rare gas mixtures. Estimations, based on collisional rate constants for Ar:He mixtures [14] and the observed efficiency of this laser [10] were in good agreement with the observed laser performance. Considering the rate constants for energy transfer in Xe [21, 22], gas mixtures of Xe with other rare gases, especially with the addition of Ar, may be suitable for efficient CW lasing. Consequently, we have investigated the suitability of a DBD for Ar($1s_5$) and Xe($1s_5$) production in mixtures of He, Ar and Xe that are of interest for OPRGL.

Experiment

The dielectric barrier discharge setup consisted of a pair of 6061 aluminum alloy electrodes 18 mm in length, cut from a square ¼×¼' profile. The electrodes were anodized in oxalic acid as described in [23], where the thickness of the alumina film was estimated to be 5-7 microns. In our experiments, the anodized layer appeared to be much thicker. Measurements of the capacitance of the electrodes, when firmly pressed together, yielded an estimate for the film thickness of 50 microns. However, this value may actually reflect surface roughness, because

estimations based on discharge power measurements (as described below) gave results close to those reported in [23].

The electrodes were mounted in a T-shaped glass cell of 50 mm outer diameter that was capped by quartz wedged windows. The cell was equipped with ports for gas input and exhaust, pressure measurement and feed-throughs for connections to the electrodes.

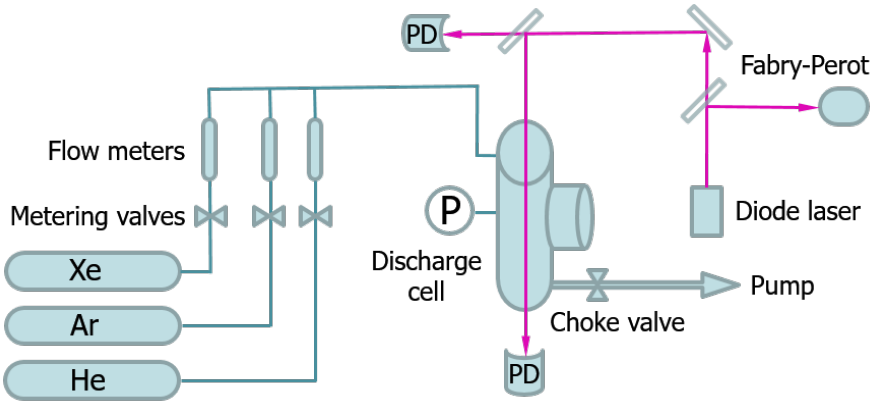

Fig. 10. Sketch of the experimental setup for metastable Ar and Xe number density measurements in a dielectric barrier discharge. P – Baratron pressure transducer, PD – photodiodes.

A sketch of the experimental setup is presented in Fig. 10. Gas mixtures were prepared with the help of metering valves and flow meters. A choke valve on the vacuum pump was used to control pressure in the cell. Gas mixture flow rates were in the range 1.5-2 slm. A commercially available PVM500 power supply operating in the range from 20 to 70 kHz in a non-resonant mode was used as the discharge driver. The power supply generated a square wave voltage through a high voltage transformer, which was connected to the electrodes without any ballast resistors. The interelectrode distance for a diffuse discharge could be as large as 5 mm and limited by design constraints. The measurements reported here were performed for distances of 2 and 3 mm. The diffuse discharge could be sustained over a wide pressure range – from a few Torr up to more than atmospheric pressure. However, the design of the cell permitted experiments only up to 750 Torr. The appearance of the discharge is shown in Fig. 11.

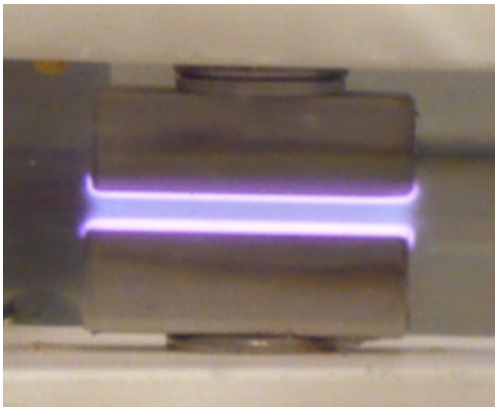

Fig. 11. Dielectric barrier discharge at an atmospheric pressure of 5%Ar in He

The [Ar($1s_5$)] and [Xe($1s_5$)] number densities were determined via optical absorption measurements using a narrow band tunable diode laser (Toptica). The discharge length (1.7 cm) and laser powers in the mW range were chosen to avoid saturation effects. For Ar, the $1s_5 \rightarrow 2p_{10}$ transition was used. Two transitions of Xe, $1s_5 \rightarrow 2p_8$ and $1s_5 \rightarrow 2p_9$ at 881.9 and 904.5 nm were used. For each measurement the diode laser scanned over the absorption line with a repetition frequency of 5 Hz, providing the mean value of [Ar($1s_5$)] or [Xe($1s_5$)] across the period of the applied voltage. Absorption line shapes were fitted to a Lorentz profile and the area (total absorbed energy) obtained as the result of the fit was used to calculate number density of metastable atoms, as described, for example, in [24].

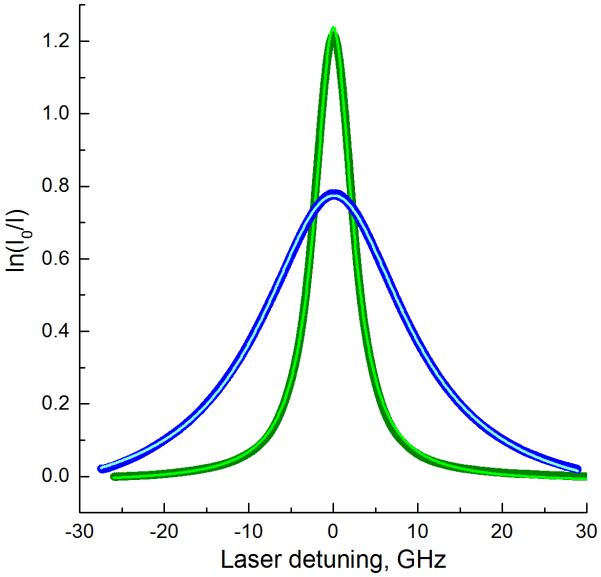

Fig. 12**.** Typical absorption line shapes of Xe 904.5 nm line obtained in 2% Xe in He mixture at 173 and 730 Torr. FWHMs are 5.4 and 21.2 GHz correspondingly. Light thin lines are Lorenz fits superimposed on dark thick lines, representing experimental data

The spectrum of Ar is easily analyzed as there is only one isotope (^{40}Ar) which has a nuclear spin of zero. Natural Xe is a mixture of several isotopes, two of which – ^{129}Xe and ^{131}Xe with almost 50% abundance, have a nonzero nuclear spin leading to a rich hyperfine structure of Xe lines. Most of those lines are grouped within 2-3 GHz from the unperturbed transition, and only two weak lines of ^{129}Xe, at 904.5 nm are 4.94 and -4.43 GHz away from the line center. However, in the pressure range 200-750 Torr, where number density measurements were performed, line shapes could be approximated as Lorentian as illustrated in Fig. 12. The Lorentz profiles obtained at different pressures were used to estimate pressure broadening. As the Doppler broadening was substantially smaller than collisional broadening in the pressure range used in these experiments, the difference between the parameters of interest from Lorentz or Voigt functions did not exceed 2-3%.

Measurements of the voltage applied to the electrodes, current and charge were performed using well-established circuitry for a barrier discharge. Low inductance thin film resistors were used for current and voltage measurements, performed with the help of a LeCroy

WaveSurfer 24Xs digital oscilloscope. Power loading into the discharge was determined using the area of Lissajous figures in the voltage/charge coordinates, which is a standard technique for this type of discharge. The largest power load attained in experiments was on the order of 10 W.

Ar:He mixtures

It was found that the interelectrode distance had a most profound effect on the metastable production and discharge properties. As an example, measurements for the 3% Ar in He mixture at 700 Torr pressure revealed the following. The electrode system with 2 mm discharge gap exhibited an almost linear increase of maximal applied voltage with current, while, for the system with a 3 mm gap, the applied voltage stayed nearly constant at 300 V for the current range from 46 to 77 mA, taken at the current maximum. At the same discharge current of 70 mA, the discharge applied voltage for the electrode system with 2 mm gap was nearly twice the value recorded for the system with a 3 mm gap. Also, for the first system the phase shift between current and voltage was not as large as for the second system, where they were almost in antiphase, as shown in figure 4. Transferred charge calculated using the amplitude of the voltage on the measuring capacitor during the cycle amounted to 480 nC for the 2 mm gap and 410 nC for the 3 mm gap.

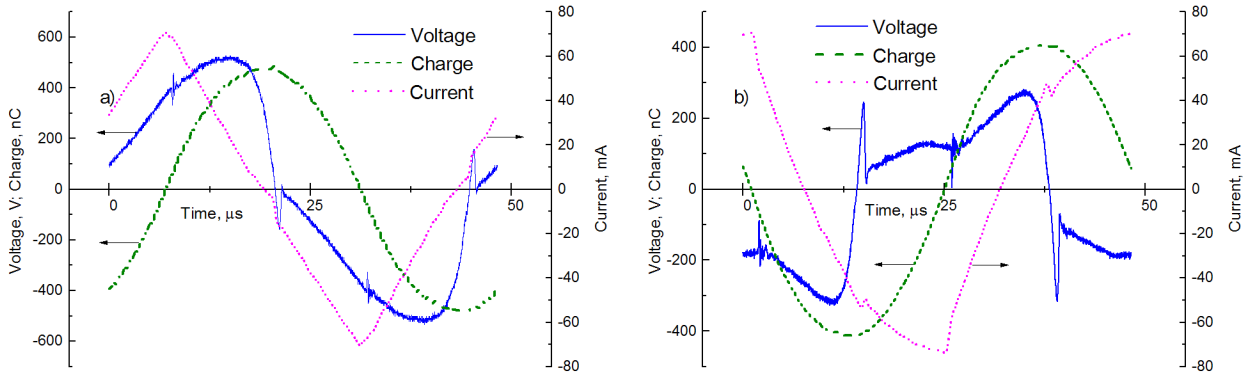

Fig. 12. Traces of applied voltage, transferred charge and discharge current through a cycle for the electrode systems with 2 a) and 3 b) mm discharge gaps. 3% Ar in He, 700 Torr.

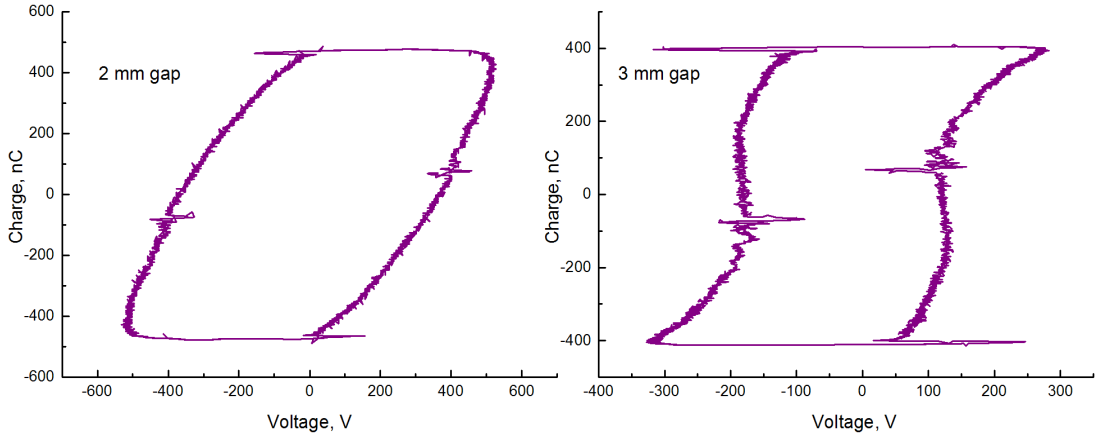

Fig. 14. Lissajous figures derived from the voltage and charge traces of Fig. 13

Lissajous figures, used to calculate power load into the discharge, are represented in Fig. 14. A constant voltage that appeared on the measuring capacitor due to asymmetry of the voltage pulses from the power supply was subtracted. Lissajous figures had qualitatively different appearances for the electrode systems with 2 and 3 mm discharge gaps, suggesting DBD operation in two different modes. However, the physical reasons for the observed discharge behavior are not clear yet and require further studies.

The power load in the discharge was almost independent of current when the discharge gap was 3 mm, while for the 2 mm gap it exhibited a linear dependence. Consequently, substantially larger number densities and more efficient production of metastables were observed in the discharge with a 2 mm gap. As shown in Fig. 15, [Ar($1s_5$)] observed in the 2 mm gap discharge was more than 3 times larger than in 3 mm gap discharge, for comparable discharge currents. Even when the discharge current was reduced by a factor of 4, the metastable number density was still larger than in the 3 mm gap discharge.

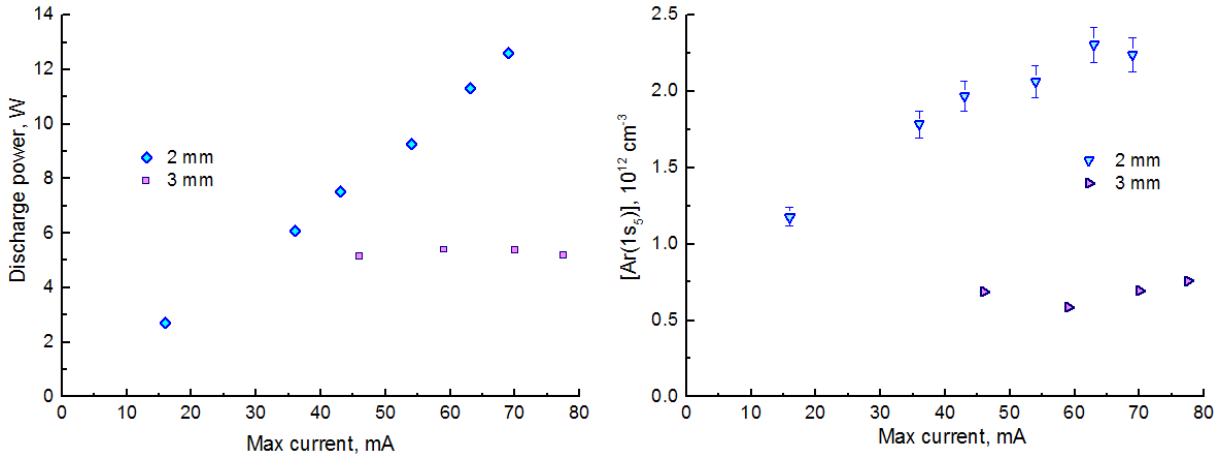

Fig. 15. Dependence of power load and mean [Ar($1s_5$)] through the amplitude cycle of the discharge current for the electrode systems with 2 and 3 mm discharge gaps.

The temporal dependence of [Ar($1s_5$)] through the period, observed with the diode laser tuned to the center of the $1s_5 \rightarrow 2p_{10}$ transition, showed that the efficiency of metastable production was quite different during adjacent half periods. The peak [Ar($1s_5$)] was at least twice the mean value measured using the tunable laser. The reason for this effect is at present unknown. Interchange of the wires from the power supply resulted in the increased production of argon metastables when positive voltage pulse was applied to the same electrode. Therefore, a possible cause might be different surface conditions of the electrodes. The thickness and porosity of the Al_2O_3 layers were not controlled during production.

The [Ar($1s_5$)] spatial distribution reported in [11] was measured by shifting the position of the discharge cell, relative to the 1 mm diameter probe laser beam. These measurements showed that the largest absorption was observed with the probe beam positioned in the middle of the discharge gap.

Measurements of the absorption line FWHM with dependence on pressure[11] were used to estimate the He pressure broadening coefficient for 912.3 nm Ar line. A value of 17 MHz $Torr^{-1}$ was determined and the observed FWHM at 700 Torr was 11.5 GHz.

Xe mixtures

In mixtures with xenon, the temporal characteristics of applied voltage, current and charge for discharge gaps of 2 and 3 mm were similar to those recorded for Ar:He mixtures. The discharge power also exhibited similar behavior.

Two Xe transitions, $1s_5 \rightarrow 2p_8$ and $1s_5 \rightarrow 2p_9$ at 881.9 and 904.5 nm, were used for number density measurements. The Einstein coefficient for the 881.9 nm line can be derived from the lifetime measurements and is well known, its value being 3.125×10^7 s^{-1}. The situation is more complicated for the 904.5 nm line because there are several allowed transitions from the $2p_9$ state. The results of several measurements were listed in [22], demonstrating a 50% uncertainty in the Einstein coefficient.

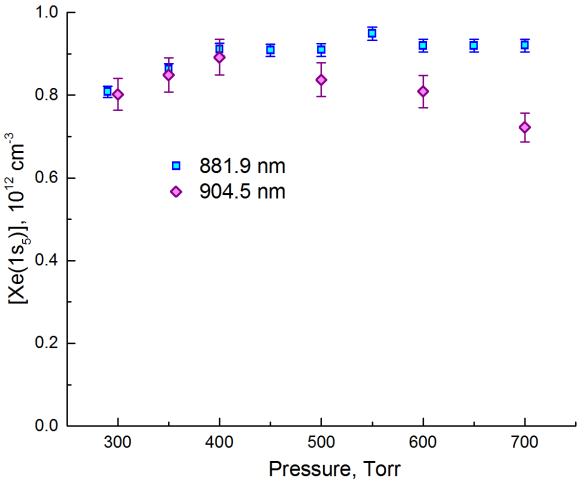

Fig. 16. Xe(1s5) number density vs pressure at a constant discharge power of 2.3 W. Discharge gap 3 mm.

In our experiments with Xe:Ne mixtures, $[Xe(1s_5)]$ was measured at a nearly constant discharge power of 2.3 W. The results are represented in Fig. 16. The best agreement between measurements at the two wavelengths was obtained when the value of Einstein coefficient for the 904.5 nm line was set to 1.24×10^7 s^{-1}. The authors of the recent studies of Xe spectra in an e-beam discharge [25] also concluded that this was the optimum value for the Einstein coefficient needed to adequately interpret their results.

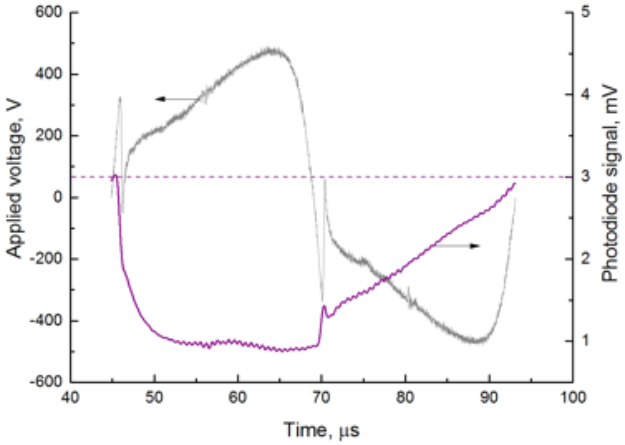

Fig. 17. Traces of applied voltage and signal from the photodiode, proportional to the transmittance of the tunable diode laser at the center of the 811.9 nm line. Dashed line is the photodiode signal with discharge off. 2 mm discharge gap, 2% Xe in He at 700 Torr, discharge power 5.7 W.

The temporal dependence of [Xe($1s_5$)] through the period was observed with the diode laser tuned to the center of the $1s_5 \rightarrow 2p_8$ transition at 811.9 nm. The results, represented in Fig. 17, again showed that the efficiency of metastable production was quite different during adjacent half periods, and the measured mean values of [Xe($1s_5$)] were substantially lower than peak number densities.

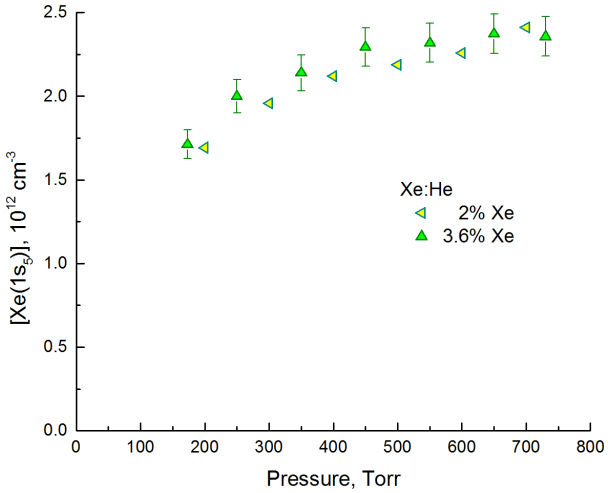

Fig. 18. [Xe(1s5)] generated in the 3 mm gap DBD discharge

The Xe($1s_5$) mean number densities achieved in the pressure range from 200 to 700 Torr in the 3 mm discharge gap are represented in Fig. 18. The discharge power varied over the range from 2.5 to 6 W. Mean [Xe($1s_5$)] values were almost three times larger than those observed for [Ar($1s_5$)] in the 3 mm gap discharge. Those results demonstrate that E/N remains large enough for efficient production of Xe metastables even at an atmospheric pressure.

For the discharge with 2 mm gap the dependence of [Xe($1s_5$)] on discharge power is represented in Fig. 19, demonstrating a weak dependence on pressure and smaller number densities, than for the 3 mm discharge gap. It is important to note that, in experiments with the

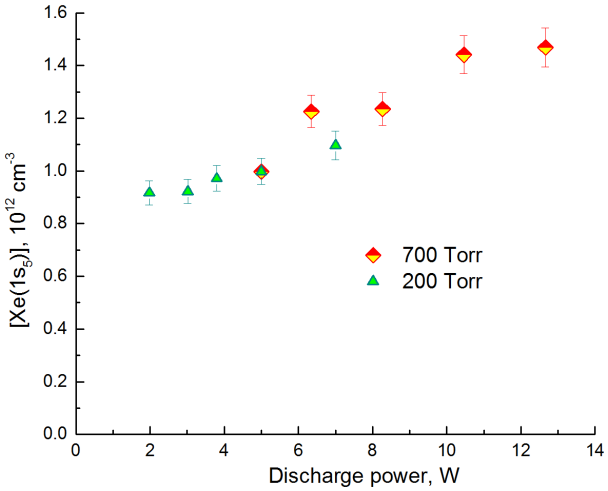

Fig. 19. Dependence of [Xe($1s_5$)] on power in the 2 mm gap discharge at two different pressures, 2% Xe in He.

2 mm gap, a new pair of electrodes was used because the original pair was damaged. Unfortunately, that resulted in smaller values of [Xe($1s_5$)], again demonstrating the dependence of the efficiency of metastables production on the surface conditions of the electrodes.

At a He pressure of 1 atm the measured Xe 904.5 nm linewidth amounted to 21 GHz. Pressure broadening coefficients in He and Ne were estimated to be 30 MHz $Torr^{-1}$ and 15 MHz $Torr^{-1}$, respectively. The larger He pressure broadening coefficient, as compared to that for the corresponding Ar line, relaxes the linewidth requirement of the diode pump source for a Xe laser.

Conclusions

Metastable number densities of the order of 10^{12} cm^{-3} were readily achieved in our experiments that utilized a 20 KHz DBD. A weak dependence of metastable number densities on pressure, and comparisons with modeling [17], suggests that in the barrier discharge with the electrodes covered with a thin Al_2O_3 layers, E/N values of the order of 10 Td or larger were realized. The temporal behavior of the Ar and Xe metastables through the DBD cycle was observed, revealing a strong dependence of the efficiency of metastable production, and therefore, E/N, on the surface conditions of electrodes. The physical reasons for this behavior are at present unknown and are the subject for further studies.

At atmospheric pressure the linewidth of the Xe $1s_5 \rightarrow 2p_9$ transition, which is used for optical pumping in the Xe OPRGL, amounted to 21 GHz. This value is almost twice that for the analogous transition in Ar, simplifying coupling with a pump diode laser. Pressure broadening coefficients for the Xe 904.5 nm were estimated to be ~30 MHz $Torr^{-1}$ (9.3×10^{-10} s^{-1} cm^{-3}) for He and ~15 MHz $Torr^{-1}$ for Ne. The results demonstrate the feasibility of using DBDs for the development of quasi-continuous optically pumped rare gas lasers.

Measurements of Rg* collisional energy transfer rate constants

The radiative decay and collisional energy transfer kinetics of the Ar* and Kr* $2p_i$ levels were characterized using time-resolved fluorescence excitation measurements [13, 14]. The fluorescence was observed along an axis that was perpendicular to the excitation laser beam, dispersed by a 0.2 m monochromator and detected by a photomultiplier tube (Hamamatsu R1767). To avoid interference from the discharge-induced emission lines, the excimer dye laser (linewidth 0.3 cm^{-1}, 10 ns pulse duration, 10 Hz repetition rate) was fired >20 μs after the discharge pulse. Time-resolved fluorescence signals were captured by using a digital oscilloscope to signal average the output from the photomultiplier. The characteristic response time of this system was determined by recording the scattered laser light. Deconvolution yielded a response time of 6.7 ns. The spectral response of the monochromator/ phototube system was calibrated by recording the emission spectrum from a tungsten halogen source.

The time-resolved fluorescence signals were analyzed by means of a master equation approach (numerical solution of the coupled rate equations). The resulting energy transfer rate constants are listed in Table 1 for Ar*+He and Ar*+Ar

Table 1. Energy transfer and quenching rate constants (10^{-11} cm^3 s^{-1}) for Ar $2p_{8,9,10}$ in collisions with Ar or He.

i	f	M	$k^M_{i,f}$	$k^M_{i,f}$	$k^M_{i,f}$
			a	*b*	*c*
8	9	Ar	1.1	1.7(3)	1.82
8	10	Ar	1.1	-	0.1
8	T	Ar	3.7	4.7(7)	-
8	q	Ar	1.5	<3	-
9	8	Ar	0.4	-	-
9	10	Ar	2.6	>1.8	0.51
9	T	Ar	5.5	5.9(4)	-
9	q	Ar	2.5	<3.5	-
10	T	Ar	0.6	2.0(6)	-
8	9	He	4.5	-	-
8	10	He	0 .4	-	-
8	T	He	4.9	-	-
8	q	He	<0.1	-	-
9	8	He	1.5	-	-
9	10	He	1.6	-	-
9	T	He	3.3	-	-
9	q	He	0.2	-	-
10	T	He	<0.005	-	-

T=total removal rate constant. q=quenching rate constant.
a. Present work, errors are ±30%. *b.* Ref. [26], numbers in parentheses are 1 errors for the least significant figure.
c. Ref [27], errors are reported as ±20%.

A sub-set of Kr*+He energy transfer rate constants was obtained by modeling the time-resolved fluorescence data. A master equation model was constructed to describe energy transfer between, and radiative relaxation from the $2p_8$, $2p_9$ and $2p_{10}$ levels. Endothermic transfer to levels above $2p_8$ was not considered as the minimum energy interval (transfer to $2p_7$) is 657 cm^{-1}. As the literature provides a range of values for the radiative lifetimes, we optimized the lifetimes in the simulations, with the constraint that they were inside the reported ranges [28]. The values used were 29, 29, and 33 ns for the $2p_8$, $2p_9$ and $2p_{10}$ levels, respectively. Based on the results for Kr*+Kr and Kr*+Xe [28, 29], the rate constants for He-induced transfer between the $2p_8$ and $2p_9$ levels were set to $k^{He}_{8,9}=2x10^{-10}$ and $k^{He}_{9,8}=1.3x10^{-10}$ cm^3 s^{-1}, with the ratio constrained by detailed balance. Transfer induced by He is probably faster than that for Kr or Xe, but, for the He pressures considered, the predicted fluorescence decay characteristics were insensitive to increases in the $2p_8 \leftrightarrow 2p_9$ rate constants. Furthermore, because thermal equilibrium was rapidly established between the $2p_8$ and $2p_9$ levels, we could not obtain independent values for the $k^{He}_{8,10}$ and $k^{He}_{9,10}$ rate constants. Hence, they were set to a common value. Fitting to the time-resolved fluorescence data for the full range of He pressures yielded an effective energy transfer rate

constant of $k^{He}_{8/9,10}=(2\pm1)x10^{-12}$ cm^3 s^{-1}. The simulations also provided an upper bound for the rate constant for population removal from $2p_{10}$ of $k^{He}_{10,T} < 5x10^{-13}$ cm^3 s^{-1}.

References for section 1

1. R. J. Beach, W. F. Krupke, V. K. Kanz, S. A. Payne, M. A. Dubinskii, and L. D. Merkle, "End-pumped continuous-wave alkali vapor lasers: experiment, model, and power scaling," Journal of the Optical Society of America B: Optical Physics **21**, 2151-2163 (2004).
2. A. V. Bogachev, S. G. Garanin, A. M. Dudov, V. A. Yeroshenko, S. M. Kulikov, G. T. Mikaelian, V. A. Panarin, V. O. Pautov, A. V. Rus, and S. A. Sukharev, "Diode-pumped cesium vapour laser with closed-cycle laser-active medium circulation," Quantum Electronics **42**, 95-98 (2012).
3. B. V. Zhdanov and R. J. Knize, "DPAL: historical perspective and summary of achievements," Proceedings of SPIE **8898**, 88980V/88981-88980V/88917 (2013).
4. F. Gao, F. Chen, J. J. Xie, D. J. Li, L. M. Zhang, G. L. Yang, J. Guo, and L. H. Guo, "Review on diode-pumped alkali vapor laser," Optik (Munich, Germany) **124**, 4353-4358 (2013).
5. G. A. Pitz, D. M. Stalnaker, E. M. Guild, B. Q. Oliker, P. J. Moran, S. W. Townsend, and D. A. Hostutler, "Advancements in flowing diode pumped alkali lasers," Proc. SPIE , High Energy/Average Power Lasers and Intense Beam Applications IX **9729**, 972902 (2016).
6. B. V. Zhdanov and R. J. Knize, "Hydrocarbon-free potassium laser," Electronics Letters **43**, 1024-1025 (2007).
7. D. W. Setser, T. D. Dreiling, H. C. Brashears, Jr., and J. H. Kolts, "Analogy between electronically excited state atoms and alkali metal atoms," Faraday Discussions of the Chemical Society **67**, 255-272 (1979).
8. J. Han and M. C. Heaven, "Gain and lasing of optically pumped metastable rare gas atoms," Opt. Lett. **37**, 2157-2159 (2012).
9. J. Han, L. Glebov, G. Venus, and M. C. Heaven, "Demonstration of a diode-pumped metastable Ar laser," Opt. Lett. **38**, 5458-5461 (2013).
10. W. T. Rawlins, K. L. Galbally-Kinney, S. J. David, A. R. Hoskinson, J. A. Hopwood, and M. C. Heaven, "Optically pumped microplasma rare gas laser," Optics Express **23**, 4804 (2015).
11. P. A. Mikheyev, J. Han, A. Clark, C. Sanderson, and M. C. Heaven, "Production of Ar metastables in a dielectric barrier discharge," XXI International Symposium on High Power Laser Systems and Applications **10254**, 102540X-102540X-102546 (2017).
12. J. Han, M. C. Heaven, D. Emmons, G. P. Perram, D. E. Weeks, and W. F. Bailey, "Pulsed discharge production Ar* metastables," in *Proc. SPIE*, High Energy/Average Power Lasers and Intense Beam Applications 2016), 97290D.
13. J. Han and M. C. Heaven, "Kinetics of optically pumped Kr metastables," Opt. Lett. **40**, 1310-1313 (2015).
14. J. Han and M. C. Heaven, "Kinetics of optically-pumped Ar metastables," Optics Letters **39**, 6541-6544 (2014).

15. D. J. Emmons and D. E. Weeks, "Kinetics of high pressure argon-helium pulsed gas discharge," Journal of Applied Physics (Melville, NY, United States) **121**, 203301/203301-203301/203311 (2017).
16. P. A. Mikheyev, "Optically pumped rare-gas lasers," Quantum Electronics **45**, 704-708 (2015).
17. A. V. Demyanov, I. V. Kochetov, and P. A. Mikheyev, "Kinetic study of a cw optically pumped laser with metastable rare gas atoms produced in an electric discharge," Journal of Physics D: Applied Physics **46**, 375202, 375208 pp (2013).
18. Z. Yang, G. Yu, H. Wang, Q. Lu, and X. Xu, "Modeling of diode pumped metastable rare gas lasers," Optics Express **23**, 13823-13832 (2015).
19. J. Gao, P. Sun, X. Wang, and D. Zuo, "Modeling of Dual-wavelength Pumped Metastable Argon Laser," Laser Physics Letters **14**, 035001 (2017).
20. F. Massines, A. Rabehi, P. Decomps, R. Ben Gadri, P. Segur, and C. Mayoux, "Experimental and theoretical study of a glow discharge at atmospheric pressure controlled by dielectric barrier," Journal of Applied Physics **83**, 2950-2957 (1998).
21. J. Xu and D. W. Setser, "Collisional deactivation studies of the xenon(6p) states in helium and neon," Journal of Chemical Physics **94**, 4243-4251 (1991).
22. W. J. Alford, "State-to-state rate constants for quenching of xenon 6p levels by rare gases," Journal of Chemical Physics **96**, 4330-4340 (1992).
23. H. I. A. Qazi, M. Sharif, S. Hussain, M. A. Badar, and H. Afzal, "Spectroscopic study of a radio-frequency atmospheric pressure dielectric barrier discharge with anodic alumina as the dielectric," Plasma Science & Technology (Bristol, United Kingdom) **15**, 900-903, 904 pp (2013).
24. S. Huebner, N. Sadeghi, E. A. D. Carbone, and J. J. A. M. van der Mullen, "Density of atoms in Ar*(3p54s) states and gas temperatures in an argon surfatron plasma measured by tunable laser spectroscopy," Journal of Applied Physics (Melville, NY, United States) **113**, 143306/143301-143306/143309 (2013).
25. V. N. Babichev, A. V. Dem'yanov, N. A. Dyatko, A. F. Pal, A. N. Starostin, and A. V. Filippov, "Experimental and theoretical study of the near IR emission of xenon excited by a fast electron beam," Plasma Physics Reports **43**, 515-532 (2017).
26. R. S. F. Chang and D. W. Setser, "Radiative lifetimes and two-body deactivation rate constants for argon(3p5,4p) and argon(3p5,4p') states," Journal of Chemical Physics **69**, 3885-3897 (1978).
27. T. D. Nguyen and N. Sadeghi, "Rate coefficients for collisional population transfer between 3p54p argon levels at 300¬∞K," Physical Review A: Atomic, Molecular, and Optical Physics **18**, 1388-1395 (1978).
28. R. S. F. Chang, H. Horiguchi, and D. W. Setser, "Radiative lifetimes and two-body collisional deactivation rate constants in argon for atomic krypton (4p55p) and atomic krypton (4p55p') states," Journal of Chemical Physics **73**, 778-790 (1980).
29. C. A. Whitehead, H. Pournasr, M. R. Bruce, H. Cai, J. Kohel, W. B. Layne, and J. W. Keto, "Deactivation of two-photon excited Xe(5p56p,6p',7p) and Kr(4p55p) in xenon and krypton," Journal of Chemical Physics **102**, 1965-1980 (1995).

Section 2
PSI Investigations of Optically Pumped Microplasma Rare-Gas Laser Dynamics

W. Terry Rawlins, Alan R. Hoskinson, Kristin L. Galbally-Kinney, Steven J. Davis
Physical Sciences Inc.

Jeffrey A. Hopwood
Tufts University

Introduction

OPRGL research at Physical Sciences Inc. (PSI) and Tufts University has continued to pursue application of linear-array microwave micro-discharges to generate metastable argon atoms and optically pumped gain in flowing Ar/He gas mixtures. We demonstrated high gain (~1 cm^{-1}) and lasing at atmospheric pressure with an optically pumped single-array microplasma,[1,2] as well as ~10x scaling of the active gain volume using a Tufts/PSI joint design for an overlapping dual-array micro-discharge-flow configuration. In dual-array discharge-flow experiments at 208 and 775 Torr, we observed transport of argon metastables out of the micro-discharge region into the bulk flow stream between the boards, with apparent metastable lifetimes of 10-20 μs at atmospheric pressure and 40-50 μs at 200 Torr.[3] We clearly observe much larger Ar($1s_5$) volume at each pressure than can be attained with the single-array discharges: ~0.02 cm^3 at 1 atm and ~0.04 cm^3 at 200 Torr, as compared to ~0.004 cm^3 at 1 atm for the 15-strip single array. At 1 atm, implementation of the dual-array discharge design totaling 14 resonators (i.e. two 7-resonator arrays) and a 1 mm array separation increases the available gain volume by a factor of 5. Given appropriate adjustments of the discharge power, power sharing, Ar mole fraction, and flow rates, it should be possible to increase the Ar($1s_5$) number densities enough to attain a gain medium with power-in-the-flow of ~0.5 W at 1 atm with this configuration. This value must be scaled by the number of times an Ar* atom can be recycled to produce laser photons. This factor is uncertain at present due to the need for better kinetics data on Ar* collisional losses, however the metastable lifetimes noted above suggest the possibility of large recycling factors for typical pump laser intensities and optical resonator configurations. These are important considerations in the design of the optical pumping architecture.

Activities at PSI and Tuft have focused on the scaling aspects of argon metastable production by the micro-strip resonator microplasmas. We have performed a complete analysis of the pressure-dependent absorption line widths observed at 912.3 nm ($1s_5 \rightarrow 2p_{10}$) during the dual-array experiments. Additional line broadening measurements and analysis were carried out at Tufts for the 811.5 nm transition ($1s_5 \rightarrow 2p_9$). The Tufts experiments used OH rotational temperature analysis to determine the gas temperatures directly, providing a rigorous test of the applicability of Lindholm-Foley theory to Ar*-He collisions. We applied the PSI steady-state saturated gain model for recent results from the Emory University laboratory, which showed significantly larger rate coefficients for Ar($1s_4 \rightarrow 1s_5$) collisional energy transfer at elevated temperatures. Application of the Emory data for representative discharge temperatures gives excellent agreement with previous PSI/Tufts results for optical gain and discharge-generated Ar($1s_5$) concentrations. We also extended the model to sub-atmospheric pressures, and found that the intrinsic gain and energy content of the optically pumped Ar*/He system at 200-300 Torr is similar to that at atmospheric

pressure. A detailed series of Ar($1s_5$) number density measurements and modeling led by Tufts observed greatly increased metastable number densities at 100-300 Torr.[4] A set of experiments conducted at PSI using a new single-array design produced optically pumped saturated laser-induced fluorescence intensities at 300 Torr indicating large Ar($1s_5$) number densities and gain in excess of 2 cm^{-1}, more than twice that observed at atmospheric pressure. Most recently, a comprehensive series of Ar($1s_5$) absorbance imaging experiments and modeling performed at Tufts has demonstrated the two-dimensional spatial distributions of argon metastable production in the micro-discharge at atmospheric and reduced pressures.[5]

Pressure Broadening: Ar($1s_5$-$2p_{10}$) transition at 912.3 nm

We examined the pressure broadening of the Ar($1s_5$-$2p_{10}$) transition at 912.3 nm. The measurements were performed in absorption by scanning a tunable diode laser across the 912 nm line in Ar/He microplasmas at various pressures. Initial measurements for single-array micro-discharges at atmospheric pressure were performed early in the program. More recently, we performed a more detailed series of measurements in the dual-array micro-discharge configuration, at pressures from 12 to 775 Torr. Similar measurements on the Ar($1s_5$-$2p_9$) transition at 811.5 nm were performed and analyzed by the Tufts group, as described further below. Detailed understanding of the line width behavior with pressure, temperature, and Ar/He mixing ratio for various pump and lasing lines is very important for models of the power scaling and for interfacing the plasma with line-narrowed diode laser pump sources.

Figure 1 illustrates the measurement configuration for the dual-array TDLS absorbance measurements. The beam from a fiber-coupled tunable diode laser, operating near 912 nm, was directed between the two arrays on a path parallel to the two discharge gaps. The Ar/He gas flow, ~4% Ar at total flow rates of 3-4 mmole/s, was confined between the boards and was directed through the 1 mm high flow channel, with the velocity vector perpendicular to the gaps. Figure 2 illustrates a side view of the Ar($2p_{10}$) emission from the upper and lower microplasmas for atmospheric and reduced pressures. Using an x-y translation stage on the fiber launch/detector assembly, the probe laser beam was traversed to various locations near the micro-discharges and in the center of the flow channel. The absorbance line shapes scanned by the laser were recorded by a digital oscilloscope. The laser scan wavelengths were determined by calibration with a Fabry-Perot etalon.

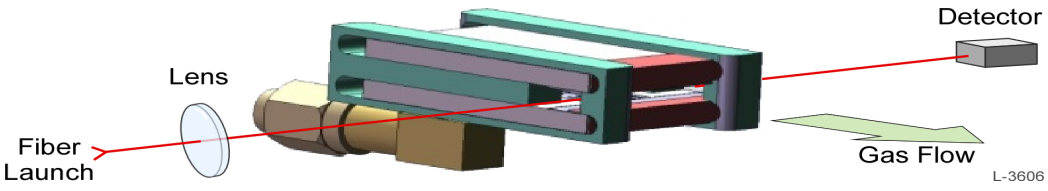

Figure 1. Schematic of dual-array micro-discharge absorbance measurements

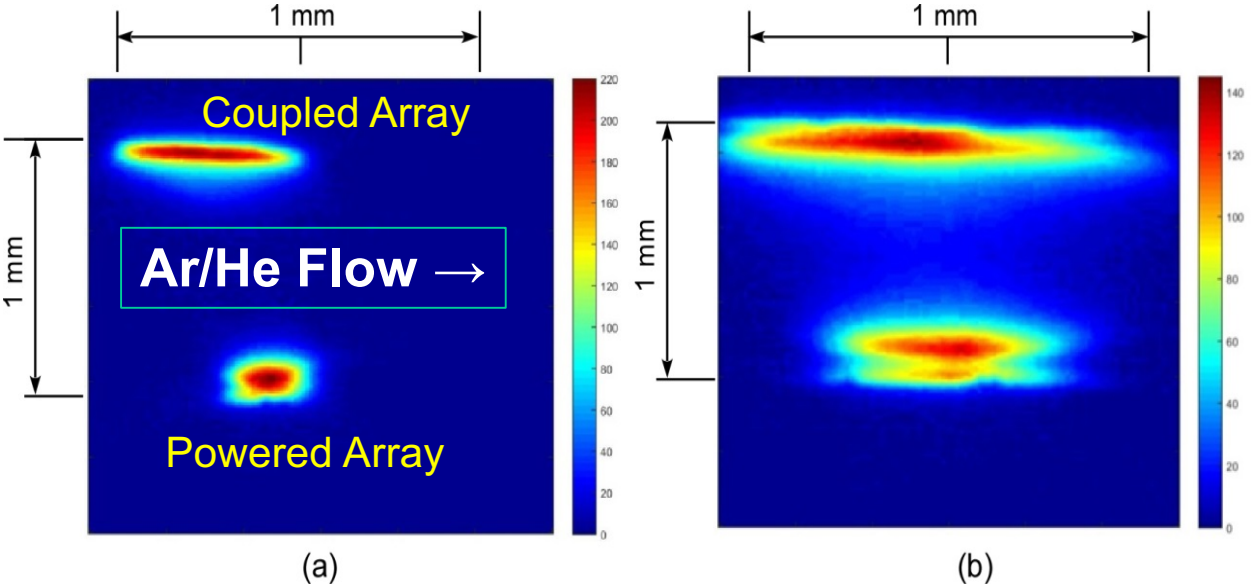

Figure 2. Side-view images of Ar($2p_{10}$) emission from dual-array microplasmas. (a) 760 Torr; (b) 229 Torr

A plot of our measured line widths is shown in Figure 3. The two data points with the single-array micro-discharge, using discharge gap widths of 25 and 100 μm, are shown at atmospheric pressure. The pressure dependent data represent two measurement columns across the dual-discharge microplasma (25 μm discharge gap, 1 mm array separation): one line of sight across the center of the flow between the boards, and another line of sight passing through the most intense part of the active micro-discharge, just above the gap on the lower (powered) array. Our expectation is that the center of the flow, which does not contain visible discharge emission at pressures above 100 Torr, has a lower temperature than the active discharge region. For each case in Figure 3, we have plotted separate linear least squares fit lines for the 200-775 and 12-100 Torr data points. The linear fits are quite good in both regimes; the slopes for the 200-775 Torr fits are noted in the figure. Given that the line width is expected to vary with temperature, and the temperature variations along the line of sight and with pressure are likely quite complex, it is surprising that simple linear behavior is observed over such a large pressure range. We have now examined the data more closely to understand the implications of these data for the temperatures in the plasma and the temperature dependence of the line widths.

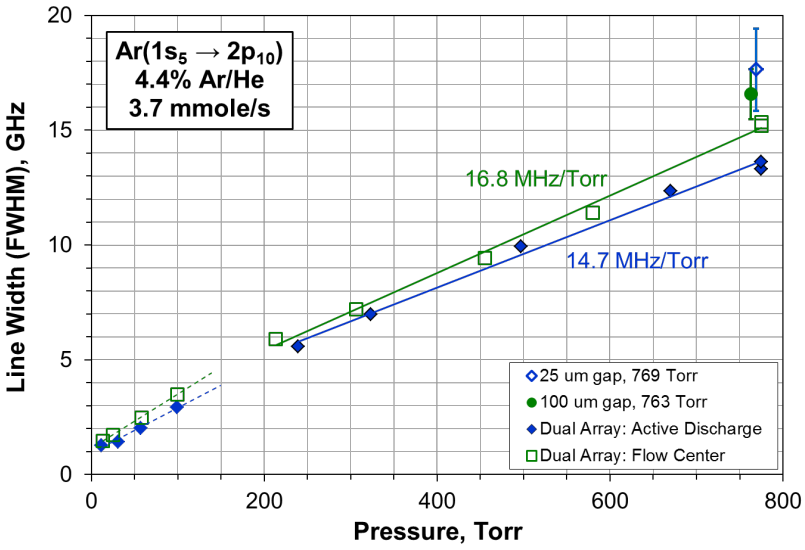

Figure 3. Line widths (full width at half maximum, FWHM) for the Ar($1s_5$-$2p_{10}$) transition at various pressures for single-array and dual-array Ar/He micro-discharges. The lines are linear least-squares fits to the dual array data sets. Slopes for the 200-775 Torr dual-array data are denoted in the figure.

We describe the formulation of the pressure-broadened Voigt line shape as the convolution of the Doppler and Lorentzian line shapes. Using the Whiting approximation, the Voigt line width (FWHM) is given by

$$\Delta\lambda_V = \Delta\lambda_L/2 + (\Delta\lambda_L^2/4 + \Delta\lambda_D^2)^{1/2}$$

where the Doppler and Lorentzian and widths are

$\Delta\nu_D = (7.16 \times 10^{-7})\ \nu_o\ (T/M)^{1/2}$, *T = temperature in K, M = molecular weight in g/mole;*

$\Delta\nu_L = P_{Torr}\ \gamma_o\ (T/T_o)^n + \Delta\nu_{TDL}$,

γ_o = pressure broadening coefficient at temperature T_o (MHz/Torr),
P_{Torr} = pressure in Torr,
$\Delta\nu_{TDL}$ = line width of the probe laser (~10 MHz)
n = -0.7 for Lindholm-Foley van der Waals impact theory (see below)

Figure 4 illustrates the scaling of the Doppler, Lorentzian, and Voigt line widths with pressure for assumed values $\{\gamma_o\ (T/T_o)^n\}$ = 17.5 MHz/Torr and T = 600 K (we examine the values of *n* and γ_o in more detail below). The Voigt line width converges to the Doppler width near 10 Torr, and is insensitive to the Doppler width above 200 Torr. Thus at low pressures, where the Doppler term is dominant, the gas temperature can be estimated from the width of the Doppler component. As shown in Figure 3, our low pressure line widths approach ~1 GHz at 12 Torr, consistent with temperatures near ~600 K at that pressure. Since most of our work to date uses >95% He diluent, we consider primarily Ar* + He collisions. We expect the gas temperature within the two fields of view to vary with pressure, as well as along each line of sight, affecting the scaling if the pressure broadening coefficient in the Lorentzian term. To examine this, we concentrate the pressure

broadening analysis on pressures 200-775 Torr, where the observed line width is essentially the Lorentzian width.

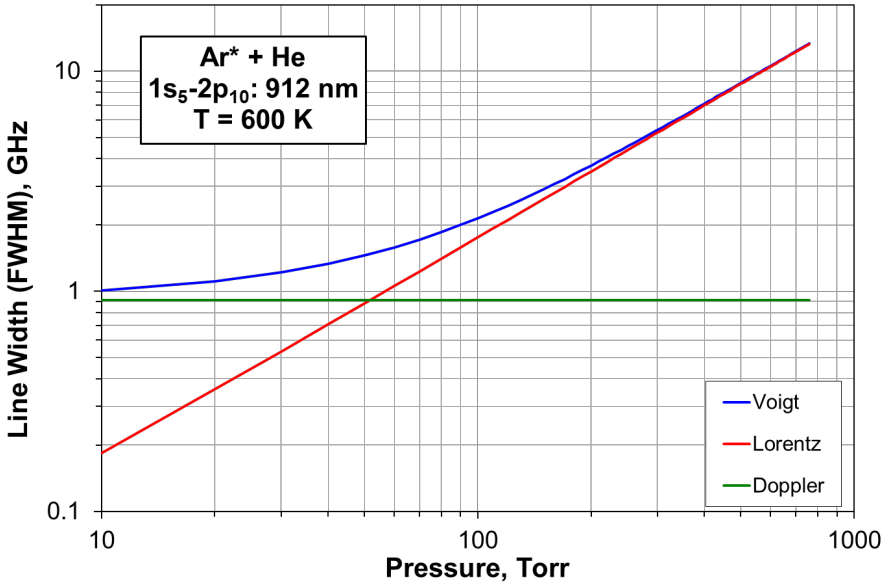

Figure 4. Scaling of Voigt line width and Doppler and Lorentzian components with pressure

Collisional line broadening characteristics depend on detailed collision dynamics and potential energy surfaces. In general terms, spectral line broadening arises from phase changes resulting from velocity changes induced when two atoms or molecules collide with each other. Hindmarsh and Farr reviewed classical and quantum theories of collision broadening for atomic systems.[6] A commonly used classical form for atom-atom collisions is Lindholm-Foley theory, which describes the collision-induced phase change in terms of an impact parameter, an average relative thermal velocity ($\bar{v}$), and a Lennard-Jones potential. Grosswendt and Witschel[7] demonstrated the applicability of this theory for collisions of closed-shell rare-gas atoms with neutral atoms having one valence electron, i.e. exactly the situation with Ar* + He and Ar* + Ar collisions. We briefly review the key elements of the derivation of the temperature scaling predicted by the theory.

The interaction potential has the familiar Lennard-Jones form:

$$V(r) = C_n/r^n - C_8/r^8 - C_6/r^6$$

where the C_6 term represents dipole-dipole attraction, C_8 represents dipole-quadrupole attraction, and C_n (n = 10 or 12) accounts for short-range quantum mechanical repulsion. As noted by Grosswendt and Witschel, experimental data for alkali-rare gas and ion-rare gas systems has shown that the C_6 term dominates the interaction and the other terms can be ignored. In this limit, the FWHM line width w reduces to

$$w = 8N\pi(3\pi/8)^{2/5}\bar{v}^{3/5}|C_6^*|^{2/5}$$
$$C_6^* = (C_6^{exc} - C_6^{ground})/\hbar$$
$$\bar{v} = (8kT/\pi\mu)^{1/2}$$

μ = *reduced mass of the colliding atom pair*
N = *number density of the perturbing gas*

In addition, the line width is related to the line-broadening cross section σ as

$$w = 2N\bar{v}\sigma$$

Then the cross section is

$$\sigma = 4\pi(3\pi/8)^{2/5}(|C_6^*|/\bar{v})^{2/5}$$

In terms of the temperature dependence, we can readily see the following:

$\sigma = \{constants\} \cdot T^{-0.2}$ *(cross section decreases weakly with increasing T)*
$w/N = \{constants\} \cdot T^{0.3}$ *(line width/number density increases weakly with increasing T)*

Hence the Lindholm-Foley theory predicts the temperature scaling of the line width:

$$w/N = w_o(T/T_o)^{0.3}$$

where w_o is the collisional broadening coefficient at the reference temperature T_o, in units of (frequency)/(number density).

Since we do not have separate determinations of the temperature in the experiments, we must translate this to the experimentally observable quantity, the pressure broadening coefficient. Substitution of $N = P/kT$ gives:

$$w/P = 2\gamma_o(T/T_o)^{-0.7}$$

where $2\gamma_o$ is the pressure broadening coefficient (for FWHM) at the reference temperature T_o, in units of (frequency)/(pressure). The theory predicts the scaling of line width with pressure and temperature noted above, with the exponent $n = -0.7$ and $2\gamma_o$ expressed in MHz/Torr. *Thus the broadening per unit pressure should decrease with increasing temperature if the collision pair conforms to Lindholm-Foley theory.*

Figure 5 shows a plot of our experimental pressure broadening coefficients at 200-775 Torr, determined at each pressure by the ratio of the line width to the pressure. The decreasing values with increasing pressure indicate an overall increase in temperature with increasing pressure. The data from the single-array cases at 1 atm indicate a slightly lower temperature than observed for the dual-array configuration. In the dual-array data, values from the center of the flow indicate a somewhat lower temperature than in the active discharge, as expected. In addition, the values in the center of the flow clearly show a complicated variation of temperature with pressure. Overall, the dual-array values decrease by a factor of ~1.6, corresponding to a temperature increase of a factor of ~2 from 200 to 775 Torr.

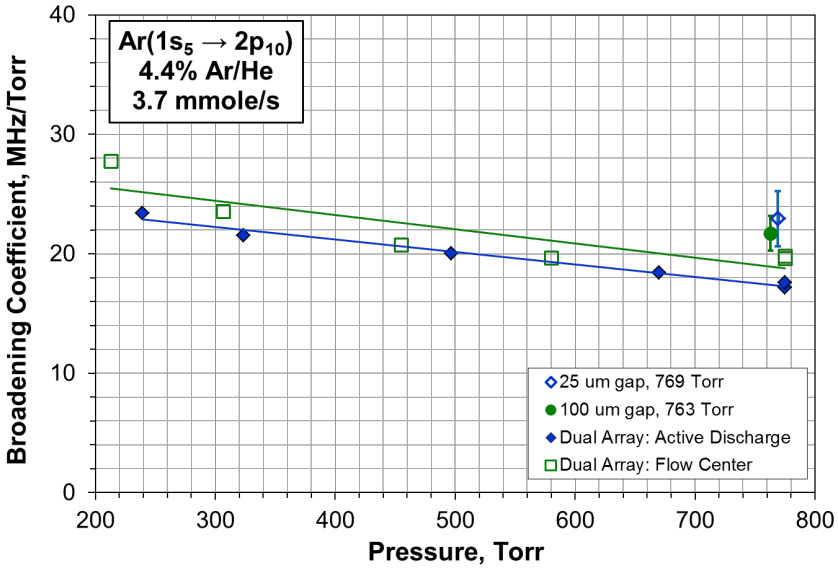

Figure 5. Pressure broadening coefficient vs. pressure, 200-775 Torr. The lines are linear least squares fits to the dual-array data sets.

Using the $T^{-0.7}$ scaling from Lindholm-Foley theory, we converted the pressure broadening coefficients into temperature ratios, T/T_o. We took the reference condition to be the higher of the two values for the dual-array flow center at 775 Torr (19.8 MHz/Torr). The results are plotted in Figure 6. Given the factor-of-two span of the relative temperature, we conclude that the temperature in the center of the flow at 200 Torr must be at least 300 K, and the temperature in the active discharge at 775 Torr must be at least 600 K.

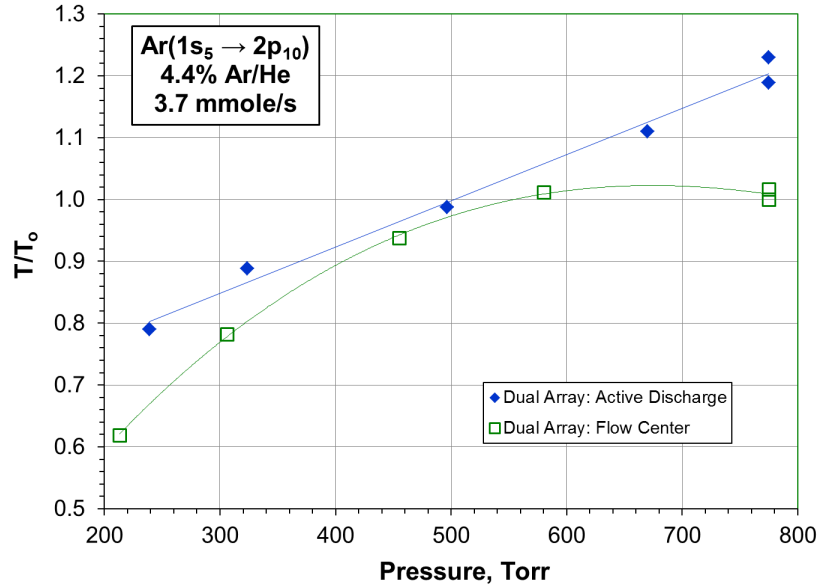

Figure 6. Relative temperatures deduced from the dual-array pressure broadening coefficients in Figure 5. The curves are least squares fits to the data.

Leiweke and Ganguly reported measurements for Ar*-Ar collisions in a diode barrier discharge at 5-30 Torr, where the temperature could be determined from the Doppler component: 24.22 MHz/Torr at 304 K for the $1s_3$-$2p_2$ transition and 22.68 MHz/Torr at 304 K for the $1s_5$-$2p_7$ transition.[8] Similarly, Perram and co-workers at AFIT[9] report smaller broadening coefficients for Ar than for He for the $1s_5$-$2p_8$ and $1s_3$-$2p_4$ lines, and larger coefficients for Ar than for He for the $1s_4$-$2p_6$ line, for estimated temperatures in the neighborhood of 400 ± 100 K; their values for the $1s_5$-$2p_8$ and $1s_3$-$2p_4$ lines are ~19 and ~23 MHz/Torr, respectively, for 5% Ar/He comparable to our 4.4% Ar/He case. Unfortunately, these results do not help us to pin down our broadening coefficients at any specific temperature along the curves. The observation of relatively large 300 K Ar*-Ar broadening coefficients for $1s_3$-$2p_2$ and $1s_5$-$2p_7$ suggest that the 300 K values for the dilute Ar/He mixture could be even larger than our values at 200 Torr, however this does not appear to be consistent with the AFIT group's results. In any event, none of these measurements address the $1s_5$-$2p_{10}$ transition investigated here. It is certainly possible that our flow temperatures are considerably greater than 300 K at 200 Torr. For example, in optically pumped gain measurements at 300 Torr in the single-array configuration, we observed $[Ar^*]/G_o$ values comparable to those at atmospheric pressure, indicating sufficiently elevated temperature (400-500 K) to drive the $1s_4 \rightarrow 1s_5$ collisional energy transfer process. Figure 7 shows a plot of the temperatures deduced assuming a reference T_o value of 500 K in the center of the flow at 1 atm; these represent lower bounds to the actual gas temperatures in the dual-discharge microplasma.

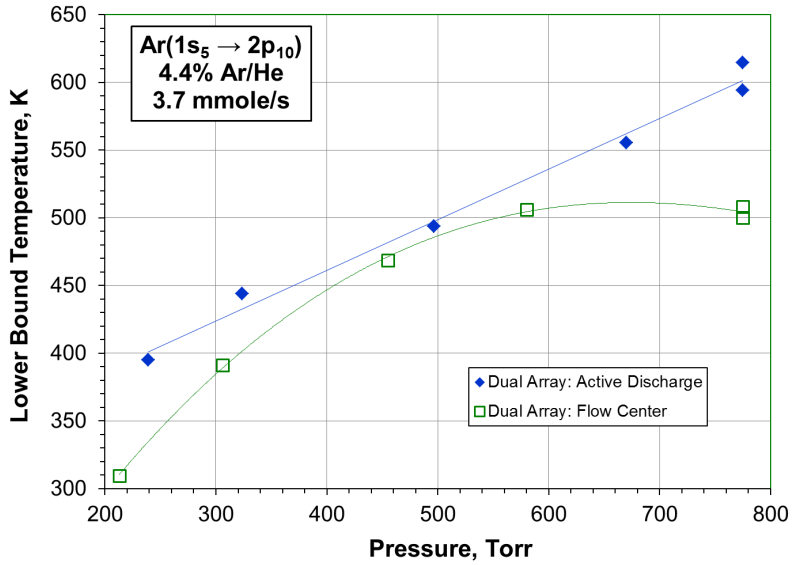

Figure 7. Lower bound temperatures estimated from the data in Figure 4. The curves are least squares fits to the data.

Model calculations of the Voigt line widths for 500 K and 600 K are compared to the data over the full pressure range in Figure 8. In each case, we matched the calculated line widths to the data at atmospheric pressure, used T_o = 500 K and γ_o = 19.8 MHz/Torr as the reference values at 775 Torr, and calculated the line widths for constant temperature over the full pressure range. It is clear that the temperatures at intermediate pressures must be reduced to match the data. Semi-empirical model calculations based on the relative temperatures (Figure 6) deduced from Lindholm-Foley scaling at 200-775 Torr are shown in Figure 9. The semi-empirical curves do not extend to the low-pressure data points, <100 Torr, which are simply fitted to least squares

lines. These results correspond to a lower bound for the Ar*-He collisional broadening coefficient of ≥1 x 10^{-9} Hz-cm^3 at 500 K, corresponding to ≥8.8 x 10^{-10} Hz-cm^3 at 300 K.

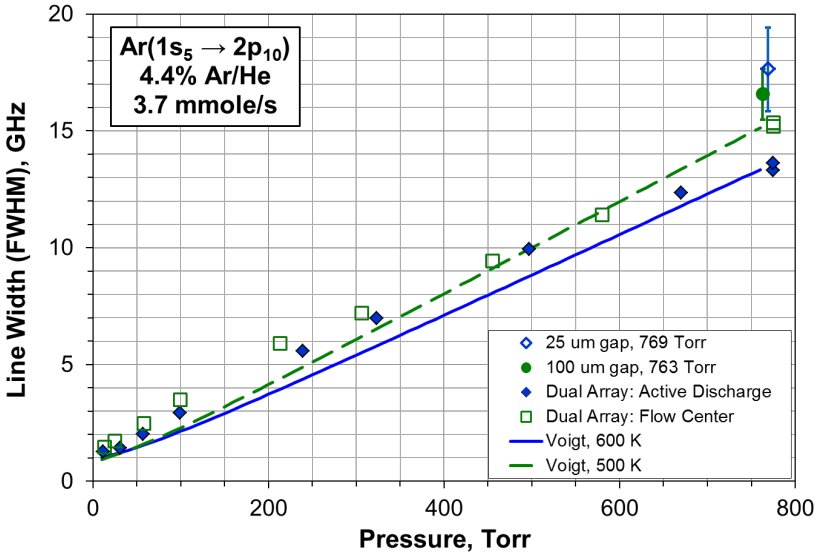

Figure 8. Comparison of line width data to Voigt model calculations for 500 K and 600 K.

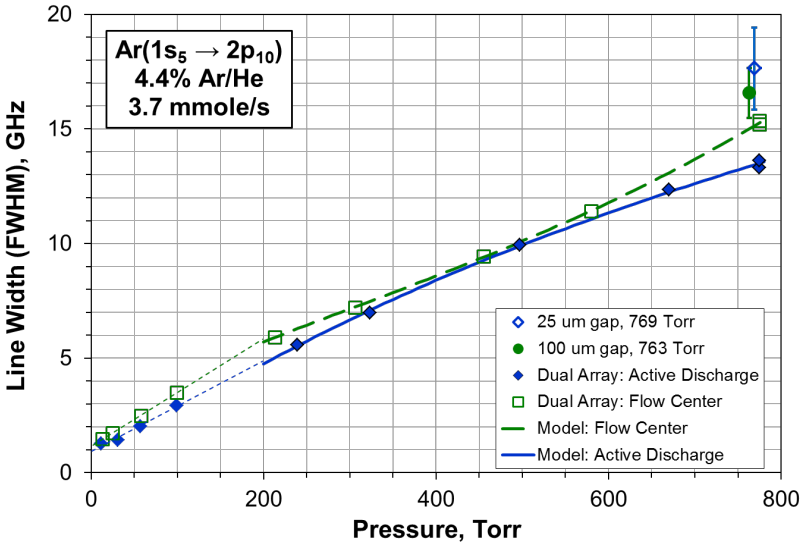

Figure 9. Comparison of line width data to semi-empirical Lindholm-Foley model calculations, using curvefits to the relative temperatures in Figure 6. Dotted lines at low pressures are linear least squares fits to the low-pressure data points (12-100 Torr).

It is important to note that Lindholm-Foley theory is an analytical approximation developed for elastic, van der Waals collisions, assuming the impact collision limit. Although widely used, the theory is directly applicable to a narrow range of collision types involving closed-shell and valence-electron atoms. If the interaction potential is more complicated than the C_6/r^6 Lennard-Jones dipole-dipole term, then the temperature dependence of the thermally averaged cross section could be significantly different from $T^{-0.2}$ as given by Lindholm-Foley theory. More rigorous theoretical treatments could consist of formulation of *ab initio* quantum

mechanical potential energy surfaces for Ar*-Ar and Ar*-He collisions, and trajectory calculations to identify the velocity dependence of the phase-changing collisions. Experimental verification requires precise temperature measurements along with the line widths, e.g. by rotational temperature analysis of emission spectra from trace diatomic species in the discharge. The line-of-sight averaging is always a limitation of the experiments; the process can only be investigated in an active discharge plasma, where the temperatures vary greatly along the measurement column.

Pressure Broadening: Ar($1s_5$-$2p_9$) transition at 811.5 nm (Tufts)

The group at Tufts (Hoskinson, Hopwood) conducted a series of pressure broadening measurements on the Ar($1s_5$-$2p_9$) transition at 811.5 nm, together with direct gas temperature measurements to provide a rigorous test of the validity of Lindholm-Foley scaling at elevated pressures. The measurements were performed in dilute Ar/He mixtures in a single-strip micro-discharge. A tunable diode laser was scanned through the absorption line and the resulting traces were analyzed using a Voigt fitting function to determine values of the FWHM as a function of pressure and discharge power. The line width measurements were accompanied by spectrally resolved measurements of trace OH($A^2\Sigma^+ \rightarrow X^2\Pi$) emission near 309 nm, using a high-resolution monochromator. The OH emission spectra were analyzed by a spectral fitting method to determine OH rotational temperatures, which were taken to be equivalent to the gas temperatures at pressures above ~50 Torr. The observed OH rotational temperatures are shown in Figure 10, for four different discharge powers. We note that the temperatures below ~50 Torr are uncertain due to low S/N and the increased possibility of rotational non-equilibrium. In general, the temperatures for these powers above 50 Torr range from 350 K to 450 K.

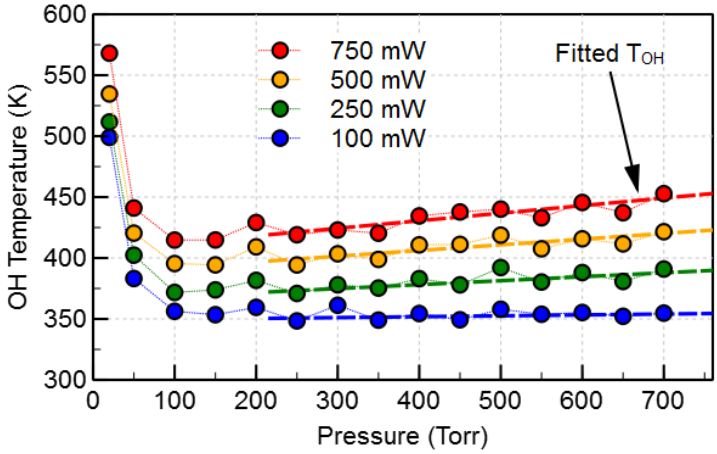

Figure 10. Observed OH rotational temperatures

The OH temperatures were applied to a Lindholm-Foley analysis as outlined above to determine the Ar*-He collisional broadening cross section for the $1s_5$-$2p_9$ transition at each experimental pressure. The results are shown in Figure 11. Disregarding the data below 50 Torr, the broadening coefficient values for 50-700 Torr are in reasonable agreement with the values determined a low pressures by Copley and coworkers[10] and by Mikheyev et al.,[11] $(6.4 \pm 0.4) \times 10^{-10}$ Hz-cm^3. There is a slight downward deviation at higher pressures, suggesting the possibility of a

departure from Lindholm-Foley theory, however this may also be within the combined range of uncertainty in the temperature and line width determinations.

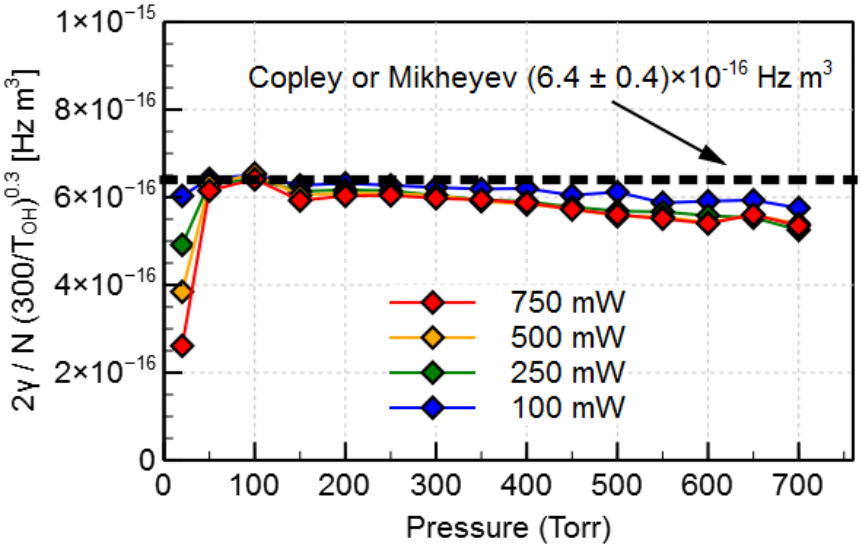

Figure 11. Ar*-He collisional broadening coefficients, $1s_5$-$2p_9$ transition (811.5 nm)

Ar* optical pumping at reduced pressure: experiments and steady-state gain model

We have conducted several series of imaging and spectral measurements to characterize Ar* in the normal and optically pumped Ar/He micro-discharge at reduced pressure, typically ~300 Torr. The experiments employed a new, fourth-generation design for the micro-discharge resonator array, with a larger discharge gap to give increased microplasma volume and a high-quality ceramic substrate material to eliminate outgassing of impurities. The optical pumping apparatus is shown in Figure 12. Mixtures of Ar and He flow along the top surface of the micro-discharge array board and across the 100 μm discharge gap, at typical flow rates of 3 to 4 mmole/s, pressures of 50-760 Torr, and typical Ar mole fractions of 1% to 5%. The micro-discharge region is probed and optically pumped by laser beams directed through the side windows, and is viewed through the top window by a high-resolution camera and an InGaAs array monochromator. In this report, we describe the analysis of laser-induced fluorescence (LIF) data to infer the optically pumped gain achieved with the new board design at reduced pressure. The results, when compared with previous results for the earlier board designs at atmospheric and reduced pressures, inform scaling concepts and provide direction for more systematic work.

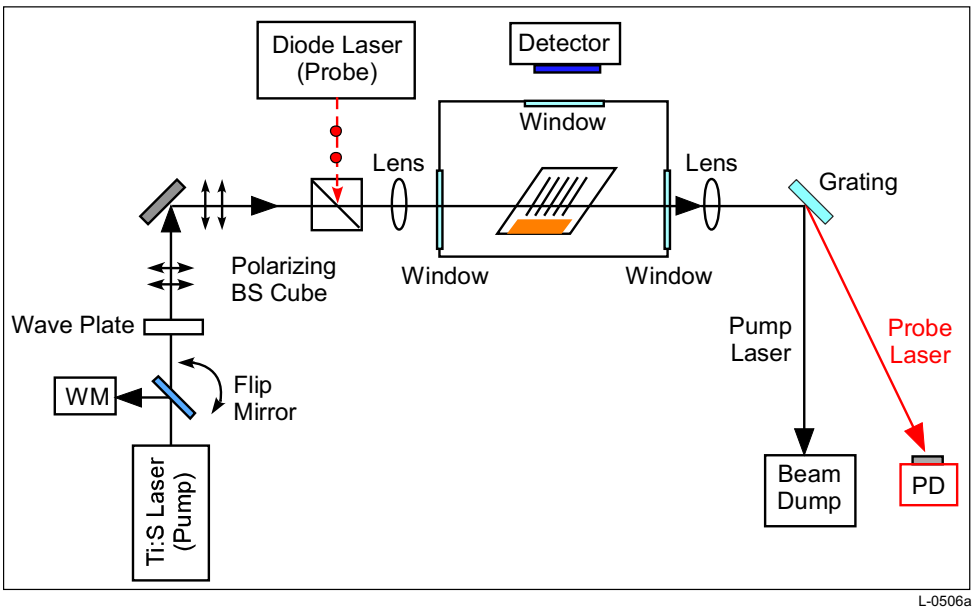

Figure 12. Schematic of microplasma OPRGL test facility.

We used laser-induced fluorescence via the Ti:S pump laser to evaluate the Ar-metastable number density and optical gains achieved with the new board design. When the pump laser intensity is high enough to fully saturate the pump transition, Ar($1s_5 \leftrightarrow 2p_9$), the number density of $2p_{10}$ determined by LIF can be used to evaluate the gain and the total Ar-metastable concentration produced in the micro-discharge. This calculation is done through the steady-state kinetics model we previously developed for this system. In the experiments, we align the pump laser beam with the discharge by viewing the discharge and LIF emission through the top window with the camera, and we acquire spectra of the natural and optically pumped micro-discharge emission through the top window with the InGaAs array monochromator. In the downlooking view, the plasma and LIF emission are optically thin for the pressure and mixture conditions of interest. As usual, the spectrometer is calibrated for absolute spectral responsivity using a NIST-traceable blackbody radiance source.

The 1 mm diameter pump laser beam was focused to the mid-point of the micro-discharge array using 1:1 imaging with a 63 mm focal length lens. The calculated beam shape within the microplasma is shown in Figure 13. The waist diameter at the focal point is 0.066 mm; the beam diameter 5 mm from the focal point is 0.10 mm. We use the 5 mm dimension to determine the average cross-sectional beam area along the field; the average power density is then 10.5 kW/cm^2 for 1 W of Ti:S power. In these experiments we used 400 mW and 700 mW of Ti:S power, corresponding to average pump power densities of 4.2 and 7.4 kW/cm^2, respectively. In the figure, the micro-discharge dimensions at 300 Torr are taken from NIR discharge imaging data.

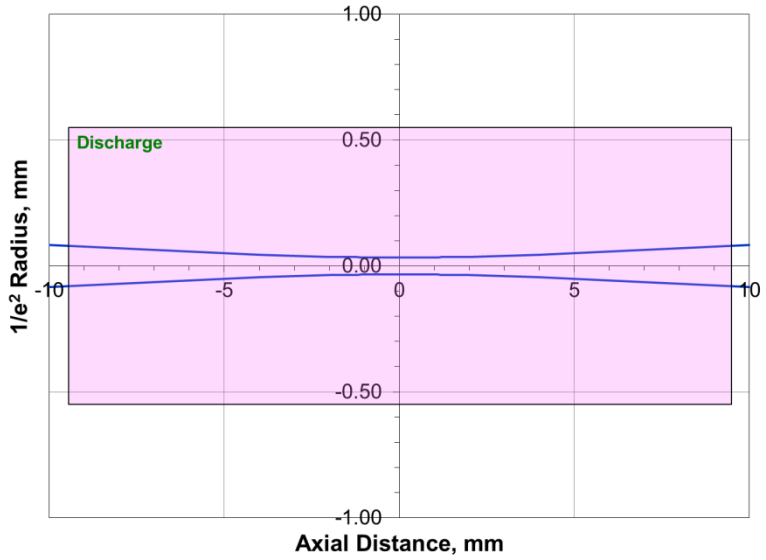

Figure 13. Illustration of the focused 811 nm pump laser beam within the microplasma volume at 300 Torr.

We acquired images and spectra for the optically pumped micro-discharge using 3% Ar/He at 3.8 mmole/s and 298 Torr. The images were acquired through the top window (Figure 12), with a field of view orthogonal to the pump laser beam, using a narrow-band filter to isolate the $2p_{10} \rightarrow 1s_5$ transition at 912 nm. Similarly, the spectra were acquired through the top window by the InGaAs array spectrometer. The Ti:S laser was aligned along the micro-discharge array using the camera to view the combination of the discharge emission and laser-induced fluorescence, and images and spectra were recorded with the pump laser off and on. Top-view images of the unpumped discharge array and the LIF volume (difference between pumped and unpumped discharge emission) are shown in Figure 14. LIF images are shown for two pump laser powers, 300 mW (~3 kW/cm^2 average) and 600 mW (~6 kW/cm^2 average). As expected from the computed beam profile, the LIF volume is much smaller than that of the microplasma, however the enhancement in the observed intensity is clearly evident. Both cases show complete penetration of the pump beam through the length of the microplasma, indicating near or full saturation of the pump transition. The LIF intensity, which is proportional to the optically pumped $2p_{10}$ number density, is somewhat greater for the 600 mW case; this indicates that the 300 mW case is not completely saturated. According to the steady-state kinetics model, once the incident pump power is high enough to completely saturate the $1s_5$-$2p_9$ pump transition, the number density of the $2p_{10}$ state (and hence the optical gain) becomes independent of pump power.

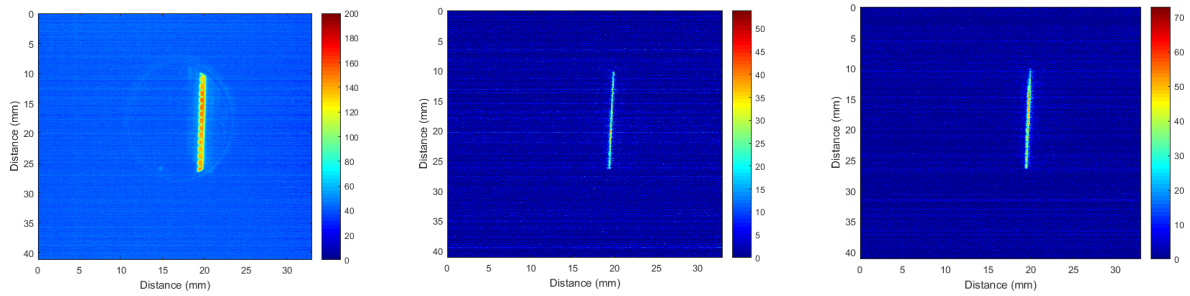

(a) (b) (c)

Figure 14. Images of microplasma and laser-induced fluorescence emission in the Ar($2p_{10}\rightarrow 1s_5$) transition at 912 nm, for 3% Ar/He at 3.8 mmole/s and 298 Torr, 7 W net discharge power. (a) Microplasma only; (b) LIF, 300 mW Ti:S power on the $1s_5\rightarrow 2p_9$ transition at 811 nm; (c) LIF, 600 mW at 811 nm

Example spectra for the unpumped microplasma and the laser-induced fluorescence for two pump powers are shown in Figure 15. The spectra were obtained using a 150 groove/mm grating giving 1.7 nm (FWHM) spectral resolution. Typical integration times were 0.1 s. The full spectrum for each case was corrected for optical transmission and instrument response determined from blackbody response calibrations, and the LIF spectra were determined by subtraction of the unpumped discharge spectrum from the laser-pumped discharge spectra. In the LIF difference spectra, the high intensity peak near 811 nm is largely due to scattered pump laser light, as well as a relatively small amount of resonance fluorescence on the $2p_9\rightarrow 1s_5$ transition. The strong LIF peaks near 912 and 966 nm are the optically pumped $2p_{10}\rightarrow 1s_5$ and $2p_{10}\rightarrow 1s_4$ transitions. The LIF spectra were obtained for Ti:S pump powers of 400 and 700 mW, corresponding to volume-averaged power densities within the microplasma of 4.2 and 7.4 kW/cm^2 respectively. The $2p_{10}$ LIF intensities for the two pump powers are essentially the same, indicating complete saturation of the pump transition at both pump power levels. We also observe very weak LIF signals from Ar($2p_8$) near 842 nm ($2p_8\rightarrow 1s_4$) and 801 nm ($2p_8\rightarrow 1s_5$). The $2p_8$ state is populated by relatively slow endoergic energy transfer from optically pumped $2p_9$, as observed by Han and Heaven:[12]

$$1s_5 + h\nu(811\text{ nm}) \leftrightarrow 2p_9$$
$$2p_9 + M \leftrightarrow 2p_8 + M$$
$$2p_9 + M \rightarrow 2p_{10} + M$$
$$2p_9 + M \rightarrow 1s_5 + M$$
$$2p_8 + M \rightarrow 2p_{10} + M$$
$$2p_8 \rightarrow 1s_4,\ 1s_5 + h\nu(842,\ 801\text{ nm})$$
$$2p_{10} \rightarrow 1s_5,\ 1s_4 + h\nu(912,\ 966\text{ nm})$$
$$1s_4 + M \leftrightarrow 1s_5 + M$$

From the peak LIF intensity ratios of 842 and 912 nm and incorporating the relative Einstein coefficients of the two transitions, we estimate $[2p_8]/[2p_{10}] \sim 0.07$. Based on steady-state kinetics and the room-temperature rate coefficients reported by Han and Heaven, we expect $[2p_8]/[2p_{10}] \sim 0.06$, in good agreement with the results. No laser-induced excitation of Ar(4p) states above $2p_8$ is evident in the LIF spectra.

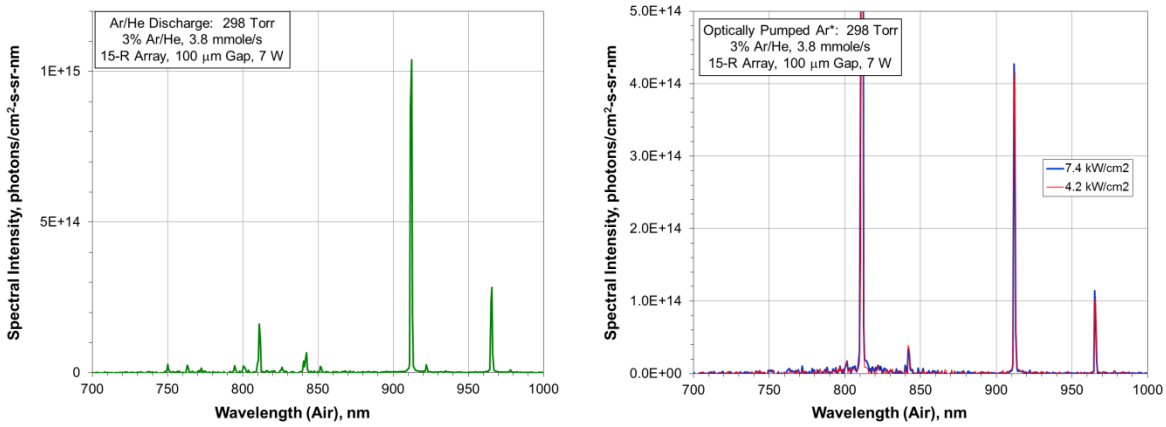

Figure 15. Response-corrected spectra for (a) Micro-discharge emission and (b) Optically pumped laser-induced fluorescence excited on the Ar($1s_5 \rightarrow 2p_9$) transition near 811 nm. Intensities are expressed per cm^2 of the field of view.

The absolute spectral intensities near 912 nm can be used to determine the number density in the $2p_{10}$ state for each case in Figure 15. This is given by the ratio of the wavelength-integrated line intensity to the path length and the Einstein coefficient:

$$[2p_{10}] = 4\pi \int I(\lambda) d\lambda \,/\, (A\ell)$$

where $I(\lambda)$ is the intensity across the $2p_{10} \rightarrow 1s_5$ line in photons/cm^2-s-sr-nm, A is the Einstein coefficient for the transition (1.89×10^7 s^{-1}), ℓ is the path length as viewed through the emitting layer, and the factor of 4π accounts for the solid angle of optically thin spontaneous emission. The effective path length is taken to be either the vertical thickness of the discharge (0.75 mm) in the case of unpumped discharge emission or the field-averaged pump beam diameter (0.10 mm) in the case of optically pumped LIF. In addition, the observed intensities are calibrated in terms of the area of the field of view, which is limited to 1 cm diameter by a collimator which is fiber-coupled to the monochromator's entrance slit; the intensity values must be corrected to account for the much smaller emitting areas in the cases of the unpumped discharge and the LIF. In effect, the integrated intensities as determined per cm^2 of the field of view must be divided by the volume of the emission and by the Einstein coefficient, and multiplied by 4π. From these considerations, we see that the focused Ti:S laser causes a ~40% increase in the total $2p_{10}$ emission intensity within the field of view, even though the optically pumped volume is only 1/80 of the micro-discharge volume. From this analysis, the $2p_{10}$ number density in the unpumped discharge is 9.4×10^{10} cm^{-3}, for 3% Ar/He, 3.8 mmole/s, 298 Torr, 7 W net discharge power.

In the optically pumped LIF spectra, the integrated intensities at 912 nm for pump powers of 400 and 700 mW are nearly the same: 6.3×10^{14} and 5.6×10^{14} photons/cm^2(FOV)-s-sr, respectively. Assuming the LIF volume is confined to the focused pump beam volume with field-averaged diameter 0.1 mm as noted above, the FOV area correction factor is $A_{LIF}/A_{FOV} = 0.013$. The volume LIF emission rates are then 6.0×10^{19} and 5.3×10^{19} photons/cm^3-s at 400 and 700 mW. Application of the $2p_{10} \rightarrow 1s_5$ Einstein coefficient gives the

optically pumped $2p_{10}$ state number densities: 3.2 x 10^{12} and 2.8 x 10^{12} cm^{-3} for 400 and 700 mW. These number densities are quite substantial and are well within the range required for high optical gain.

Ar* optical pumping: PSI steady-state kinetics model

We devised a simple steady-state kinetics model to evaluate the CW saturated gain.[1-3] The model is illustrated in Figure 16, which shows the four primary states involved in the optical pumping process. We have also included the minor effects of the $2p_8$ state, which is populated to a small degree by upward energy transfer (154.5 cm^{-1}) from $2p_9$, so the model is effectively a five-state model. The kinetics model is illustrated with excitation and deactivation rates corresponding to the reaction set listed above. Levels 1, 2, 3 and 4 represent the Ar $1s_5$, $2p_{10}$, $2p_9$, and $1s_4$ states respectively. In this scheme, level 1 is optically excited to level 3, which is collisionally coupled to level 2, creating a population inversion between levels 2 and 1. I is the excitation laser intensity transmitted by the medium, B_{13} and B_{31} are the absorption and stimulated emission coefficients for 1↔3, A_{31} is the Einstein spontaneous emission coefficient for 3→1, k_c is the rate coefficient for collisional energy transfer from 3 to 2, $[M]$ is the number density of the bath gas (He in our case), A_{21} is the Einstein spontaneous emission coefficient for 2→1, k_Q is the rate coefficient for quenching of $2p_9$ to $1s_5$, B_{12} and B_{21} are the absorption and stimulated emission coefficients for 1↔2, and I' is the transmitted intensity of stimulated emission from 2 to 1. For the case of open-loop gain (no mirrors or lasing), the 1↔2 stimulated emission terms can be neglected.

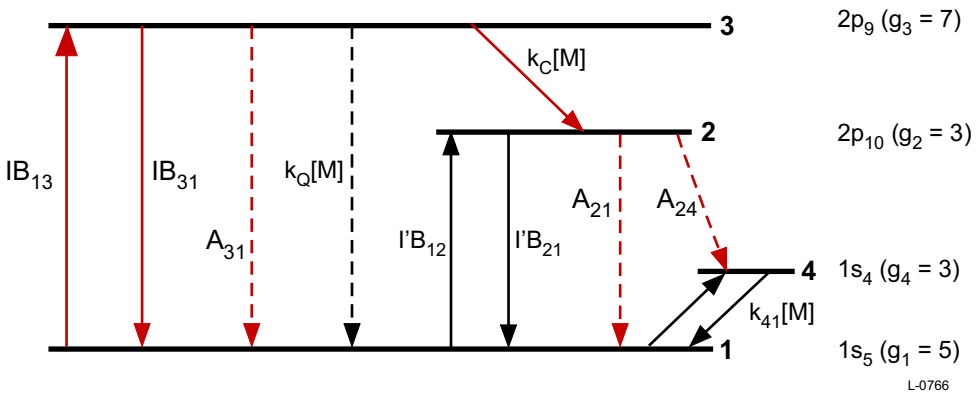

Figure 16. Illustration of radiative and collisional processes included in the PSI steady-state model for continuous-wave saturated gain in the absence of lasing

The value of k_c is determined by steady state between $2p_9$ and $2p_8$. At pressures of ~300 Torr and above, this relationship is independent of pressure and is given by:

$$k_c = k_{9\to10} + \{k_{9\to8}/(k_{8\to9} + k_{8\to10})\}k_{8\to10} \approx k_{9\to10} + 0.3k_{8\to10}$$

To incorporate the fourth state, $1s_4$, we have added A_{24}, the Einstein coefficient for 2→4 emission, k_{41}, the rate coefficient for collisional energy transfer from $1s_4$ to $1s_5$, and k_{14}, the reverse rate coefficient determined by detailed balance (the energy of the $1s_4$ state of Ar is 606.83 cm^{-1} above that of $1s_5$). For completeness, we have also included A_{40}, the effective radiative loss rate of $1s_4$ through the strongly allowed resonance transition to the ground state. However, this transition is optically thick over a dimension of a few microns for our experimental conditions, and thus the $1s_4$

state population is radiatively trapped. Han and Heaven[12] observed an effective radiative loss rate of (4 to 6) x 10^5 s^{-1} for this state, which is small compared to the collisional coupling terms.

The detailed steady-state equations for non-lasing optical excitation are as follows:

$$n_3 = \frac{IB_{13}}{IB_{31} + A_{31} + \left(k_c + k_Q\right)[M]}\, n_1$$

$$n_2 = \frac{k_c[M]}{A_{21} + A_{24}}\, n_3$$

$$n_1 = \frac{\left(IB_{31} + A_{31} + k_Q[M]\right) n_3 + A_{21} n_2 + k_{41}[M]\, n_4}{IB_{13} + k_{14}[M]}$$

$$n_4 = \frac{A_{24} n_2 + k_{14}[M]\, n_1}{k_{41}[M] + A_{40}}$$

$$n_{TOT} = n_1 + n_2 + n_3 + n_4$$

$$I = \frac{I_0}{\delta\nu}\int_O^L \exp\left(-\sigma_{13} N_{13} z\right) dz, \;\; N_{13} = n_1 - \frac{5}{7} n_3$$

We have incorporated the room-temperature collisional energy transfer rate coefficients for M = He as reported by Han and Heaven,[12] as well as their subsequent value for k_{41} at elevated temperature near 600 K, together with NIST-tabulated values for the relevant Einstein coefficients. Analysis of our $1s_5 \rightarrow 2p_{10}$ pressure broadening data indicates that the gas temperature at 300 Torr is ~450 K (~6.9 GHz FWHM line width). The resulting values are k_c = 1.7 x 10^{-11} cm^3/s, k_{41} = 4.4 x 10^{-13} cm^3/s at 450 K (from an Arrhenius fit to the data of Han and Heaven), A_{31} = 3.31 x 10^7 s^{-1}, A_{21} = 1.89 x 10^7 s^{-1}, and A_{24} = 5.43 x 10^6 s^{-1}.

The steady-state solution contains six equations and six unknowns as shown above. Due to the coupling of the transmitted pump intensity to the populations n_1 and n_3, the set of simultaneous equations is transcendental, and must be solved by an iterative process. For present purposes, we focus on the solution for the saturated (bleached) condition, where the pump intensity I is so large that the stimulated emission terms IB_{31} and IB_{13} overwhelm the spontaneous emission and collisional deactivation rates for n_1 and n_3. In this limit, we have $n_3/n_1 = B_{13}/B_{31} = g_3/g_1 = 7/5$, the medium is essentially transparent to the pump beam, and the state populations and optical gain are independent of pump intensity. If we define $n_{TOT} = [Ar^*]_o$, the total $Ar(1s_5)$ number density produced by the discharge in the absence of laser pumping, then the relative state number densities are given as follows:

$$n_3/n_1 = 7/5$$

$$n_2/n_1 = (n_3/n_1)(n_2/n_3)$$

$$n_2/n_3 = k_c[M] / (A_{21} + A_{24})$$

$$n_4/n_1 = \{(n_2/n_1)A_{24} + k_{14}[M]\} / \{k_{41}[M] + A_{40}\}$$

$$n_{TOT}/n_1 = 1 + n_2/n_1 + n_3/n_1 + n_4/n_1$$

$$[Ar^*]_o/G_o = n_{TOT}/G_o = \{n_{TOT}/n_1\} / \{\sigma_{12}(5/3)(n_2/n_1) - 1\}$$

The $1s_5 \rightarrow 2p_{10}$ absorption cross section in the gain equation, σ_{12}, is evaluated from A_{21} using the appropriate pressure-broadened line width as determined above. From this set of equations at 300 Torr and 450 K, we determine $n_2/n_1 = 6.37$, $n_4/n_1 = 9.75$, $n_{TOT}/n_1 = 17.06$, and $[Ar^*]_o/G_o = 3.25 \times 10^{12}$ cm^{-2}. The n_2/n_1 and n_{TOT}/n_1 values give $n_{TOT}/n_2 = [Ar^*]_o/[2p_{10}] = 2.68$. For the LIF measured value $[2p_{10}] \approx 3 \times 10^{12}$ cm^{-3}, the model indicates $[Ar^*]_o \approx 8 \times 10^{12}$ cm^{-3} and $G_o \approx 2.5$ cm^{-1}. As a crosscheck, a similar analysis assuming a temperature of 600 K (as observed at 1 atm) gives $[Ar^*]_o \approx 6 \times 10^{12}$ cm^{-3} and $G_o \approx 2.4$ cm^{-1}.

The results for $[Ar^*]_o$ and gain are much larger than we observed in previous direct gain probe experiments at reduced pressure with the "Gen-2" duroid board and 100 μm gap.[3] However, the inferred Ar[$1s_5$] number densities are consistent with observations at Tufts by Hoskinson et al.[4] of 8-10 x 10^{12} cm^{-3} at 300 Torr, low Ar mole fraction, and much lower discharge power (see below). The most significant potential source of error in the data analysis is the evaluation of the field-of-view correction factor, A_{LIF}/A_{FOV}, which is very sensitive to details of the optical alignment. If the fiber-coupled collimator is misaligned with respect to the discharge gap, then the intercepted A_{LIF} would be smaller than assumed. If the collimator is positioned too far from the window, then the field of view A_{FOV} could be larger than expected. Either of these errors would result in a *smaller* correction factor, leading to *larger* values for $[2p_{10}]$, $[Ar^*]_o$, and gain. Thus it appears that the values determined in this analysis are likely to be *lower bounds*. Clearly, these results need to be confirmed by direct TDL probing of the $1s_5$-$2p_{10}$ absorbance and optical gain. However, the implications of these results for OPRGL development are very enlightening, and suggest significant advantages in operation at reduced pressures.

In separate experiments performed at Tufts, Hoskinson et al. measured Ar($1s_5$) number densities in a single-resonator Ar/He micro-discharge as functions of Ar mole fraction and total pressure.[4] A snapshot of some of their results is shown in Figure 17. At the nominal preferred dilution level of ~5% Ar, they observed pronounced increase in Ar($1s_5$) number density with decreasing pressure, from ~5 x 10^{12} cm^{-3} at 730 Torr (consistent with values observed at PSI[1-3] at atmospheric pressure), to ~10^{13} cm^{-3} at 300 Torr, to even larger values at 100 Torr. These observations are consistent with the results described above, and suggest increased gain at reduced pressures.

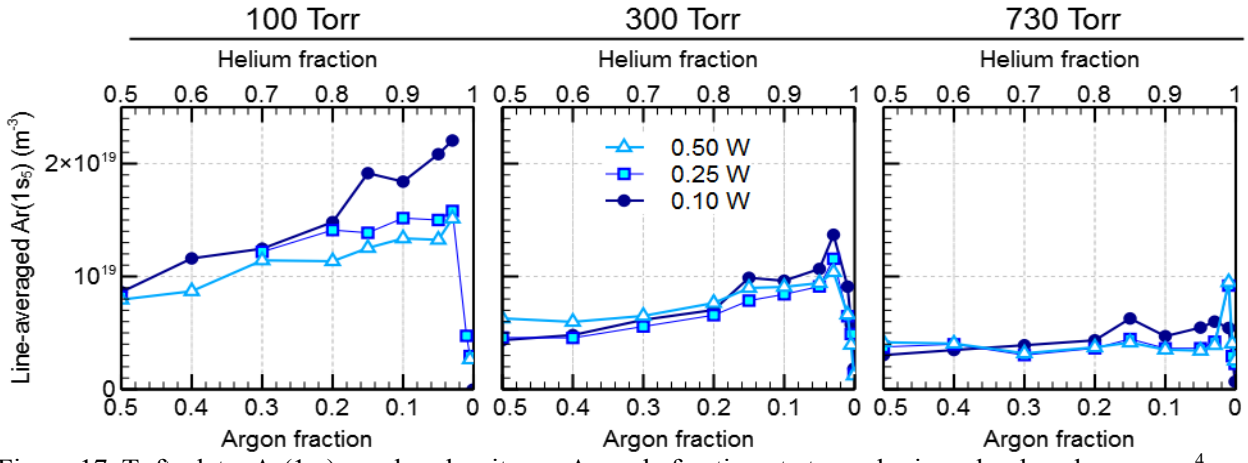

Figure 17. Tufts data: Ar($1s_5$) number density vs. Ar mole fraction at atmospheric and reduced pressures[4]

To pursue this point further, we used the steady-state gain model to explore the pressure dependence of the optically pumped state populations and the gain parameter $[Ar(1s_5)]_o/G_o$. We used the data from the dual-array discharge experiments to describe the pressure dependence of the temperature and line width. The results are shown in Figure 18. The curves were calculated for two cases of the dual-array configuration: the active micro-discharge, where the temperatures are higher, and the neutral discharge effluent, where the temperatures are somewhat lower (see Figure 7). Also plotted is the previous experimental observation by Rawlins et al. at atmospheric pressure.[1-3] The model indicates that the intrinsic gain parameter is almost the same at 300 Torr as it is at atmospheric pressure. Thus, if much larger metastable number densities can be achieved at reduced pressures, the optical gain should be much larger, in keeping with the factor-of-two increase in gain implied by our LIF results at 300 Torr. Given the additional advantage of significantly larger microplasma volume and increased $Ar(1s_5)$ collisional lifetime, low-pressure operation may offer significant advantages for OPRGL scaling.

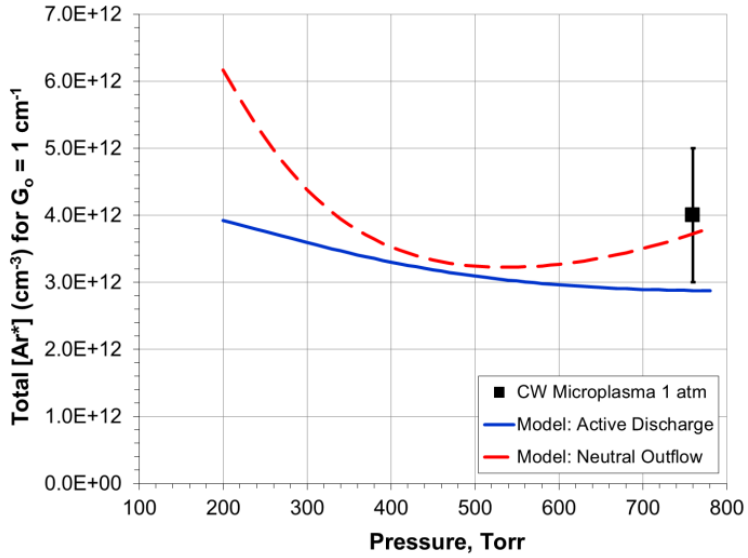

Figure 18. Steady-state model predictions of $[Ar(1s_5)]_o/G_o$ vs. pressure

Conclusions

The research groups at PSI and Tufts investigated the optically pumped microplasma rare-gas laser, with focus on several aspects related to power scaling. These included absorption and gain measurements with single-array microplasmas, and the first volume scaling investigations with a new dual-array configuration. Many of these experiments were exploratory in nature, and produced preliminary data which needs to be verified through further work. Nevertheless, the results support a number of conclusions and research directions:

- The most important scaling requirement is increasing the gain volume. This is especially important at 1 atm, where the micro-discharge approach is uniquely suited for sustaining CW discharges. Using a dual-array micro-discharge configuration, we have demonstrated the feasibility for scaling up the gain volume using a multi-array, flow-through design.

- Another critical parameter is the collisional lifetime of $Ar(1s_5)$ once it leaves the active discharge. Although further analysis is required, our data to date indicate that the post-discharge $Ar(1s_5)$ lifetime is relatively short, consistent with rapid three-body excimer formation. This suggests that a scaled concept may require optical pumping within or at the edge of the active discharge volume. The recycling multiplier needs to be evaluated from modeling of the excitation and lasing kinetics.

- Reduced pressures offer favorable gain conditions and larger microplasma volumes. Operation at 200-500 Torr may have significant advantages for scaling the gain volume, however there are obvious disadvantages for matching the absorption line widths to those of state-of-the-art diode pump lasers. Additional investigations at reduced pressures are needed to guide evaluations of these trade-offs.

- Our experiments provide empirical pressure-dependent, line-of-sight averaged absorption line widths for our specific discharge conditions and optical transitions, as do those of the Tufts and AFIT groups. For scaling analyses, the temperature dependence of the pressure broadening term needs to be determined, by experiment and/or theory.

- The empirical ratio of discharge-generated, unpumped $Ar(1s_5)$ number density to the saturated gain appears to be a robust performance and scaling metric which correlates to the collisional state coupling dynamics through a simple steady-state kinetics model.

- The high energy content of the microplasma-generated Ar* flow supports laser output scaling to the 100 kW range with only a few liters of active gain volume and operation near atmospheric pressure. Our observed micro-discharge and optical efficiencies are reasonably consistent with published power scaling models.[13,14] Through modest increases in the micro-discharge volume via a flow-through multi-array approach, scaling to a few W should be a feasible first endeavor.

References for section 2

1. W.T. Rawlins, K.L. Galbally-Kinney, S.J. Davis, A.R. Hoskinson, J.A. Hopwood, and M.C. Heaven, "Optically pumped microplasma rare gas laser," Opt. Express 23, 4804-4813 (2015).
2. W.T. Rawlins, K.L. Galbally-Kinney, S.J. Davis, A.R. Hoskinson, and J.A. Hopwood, "Laser excitation dynamics of argon metastables generated in atmospheric pressure flows by microwave frequency microplasma arrays," Proc. SPIE 8962-2, High Energy/Average Power Lasers and Intense Beam Applications VII, San Francisco CA, February 2014.
3. W.T. Rawlins, K.L. Galbally-Kinney, S.J. Davis, A.R. Hoskinson, and J.A. Hopwood, "Laser excitation dynamics of argon metastables generated in atmospheric pressure flows by microwave frequency microplasma arrays," Proc. SPIE 9729-10, High Energy/Average Power Lasers and Intense Beam Applications IX, San Francisco CA, February 2016.
4. A.R. Hoskinson, J. Gregorio, J. Hopwood, K. Galbally-Kinney, S.J. Davis, and W.T. Rawlins, "Argon metastable production in argon-helium microplasmas," J. Appl. Phys. 119, 233301 (2016).
5. A.R. Hoskinson, J. Gregorio, J. Hopwood, K. Galbally-Kinney, S.J. Davis, and W.T. Rawlins, "Spatially-resolved modeling and measurements of metastable argon atoms in argon-helium microplasmas," in preparation for J. Appl. Phys., 2016
6. W.R. Hindmarsh and J.M. Farr, "Collision Broadening of Spectral Lines by Neutral Atoms," Prog. Quantum Elect. 2, 141-214 (1973)
7. B. Grosswendt and W. Witschel, "Calculation of Line Broadening Cross Sections for Level Crossing Experiments in Alkali-Rare Gas Systems," Z. Naturforsch. 29a, 605-609 (1974)
8. R.J. Leiweke and B.N. Ganguly, "Diode laser spectroscopic measurements of gas temperature in a pulsed dielectric barrier discharge using collisional broadening and shift of $1s_3$-$2p_2$ and $1s_5$-$2p_7$ argon transitions," J. Appl. Phys. 113, 143302 (2013)
9. B. Eshel, C.A. Rice, and G.P. Perram, "Pressure broadening and shift rates for Ar(s-p) transitions in an Ar-He discharge," J. Quant. Spectrosc. Radiat. Transfer 179, 40-50 (2016).
10. C.S. Lee, D.M. Camm, and G.H. Copley, "Van der Waals broadening of argon absorption lines," J. Quant. Spectrosc. Radiat. Transfer 15, 211-216 (1975).
11. P.A. Mikheyev, A.K. Chernyshov, N.I. Ufimtsev, E.A. Vorontsova, and V.N. Azyazov, "Pressure broadening of Ar and Kr $(n+1)s[3/2]_2 \rightarrow (n+1)p[5/2]_3$ transition in the parent gases and in He," J. Quant. Spectrosc. Radiat. Transfer 164, 1-7 (2015).
12. J. Han and M.C. Heaven, "Kinetics of optically pumped Ar metastables," Optics Letters 39, 6541-6544 (2014)
13. A.V. Demyanov, I.V. Kochetov, and P.A. Mikheyev, "Kinetic study of a cw optically pumped laser with metastable rare gas atoms produced in an electric discharge," J. Phys. D: Appl. Phys. 46, 375202 (2013).
14. Z. Yang, G. Yu, H. Wang, Q. Lu, and X. Xu, "Modeling of diode pumped metastable rare gas lasers," Opt. Express 23, 13823-13832 (2015).

Diode Pumped Rare Gas Lasers

High Energy Laser Joint Technology Office
Multi-Disciplinary Research Initiative

AFIT Progress Report

18 October 2016

Professor Glen Perram
Department of Engineering Physics
Air Force Institute of Technology
Wright-Patterson Air Force Base, OH 45433-7765

glen.perram@afit.edu, (937)-255-3636 x 4504

1. Introduction

The Air Force Institute of Technology supported a High Energy Laser Joint Technology Office, Multi-Disciplinary Research Initiative led by Emory University to investigate diode pumped rare gas lasers. AFIT worked on the development of a large volume, high metastable density discharge, studied line shape kinetics, developed a discharge model, and examined intensity scaling.

Major accomplishments include:

a. The saturation behavior of the Ar$1s_5$ level was studied using pump-probe spectroscopy. A manuscript has been prepared for submission to Optical Communications.

b. The discharge produced populations in the p-states were measured using optical emission and diode laser absorption spectroscopy. Lt Owens successfully defended his MS thesis on this topic in March 2016. An oral presentation entitled "Rare gas laser kinetics" by Steven A. Owen, Ben Eshel, Christopher A. Rice and Glen P. Perram was delivered at the annual Directed Energy Professional Society.

c. A micro-cathode sustained discharge array has been operated at modest pressure and the fluorescence fills the 1 cm gap.

d. A high pressure argon discharge has been developed using a cylindrical anode/cathode.

e. A five-level laser model has been in developed to describe the observed population distributions in the high-volume, atmospheric pressure radio-frequency discharges both with and without optical pumping.

2. Technical Accomplishments

a. Laser saturation spectra for Ar $1s_5$

The saturation behavior of the Ar($1s_5$) level was studied using pump-probe spectroscopy where the $1s_5$ - $2p_9$ transition is strongly pumped and the $1s_5$ - $2p_8$ transition is probed by a weak laser. The observed spectra show hole burning with width and depth dependent on the pump laser power and behave, qualitatively, as expected. An analytic line shape for highly saturated transitions was modified to account for the influence of a spatially varying pump and probe laser profile as well as that of velocity-changing collisions by introducing two independent saturation parameters. The two saturation intensities derived from the saturation parameters were shown to be in reasonable agreement with the zero-pressure saturation intensity and the rate-equation derived saturation intensity.

Absorbance spectra for the $1s_5 - 2p_8$ transition at 801.699 nm were measured for laser powers of 0 to 800 mW at pressures of 5, 10, 50 and 100 Torr. Figure 1 shows spectra in the absence of a pump laser for all four pressures. The line shapes show the expected trend of a broadening and red-shift caused by Ar-Ar collisions. Upon integrating the absorbance and solving for the number densities, we find that the number densities are 7.4, 9.1, 7.0, and 8.3 x 10^{11} cm^{-3} for the pressures 5, 10, 50 and 100 Torr, respectively.

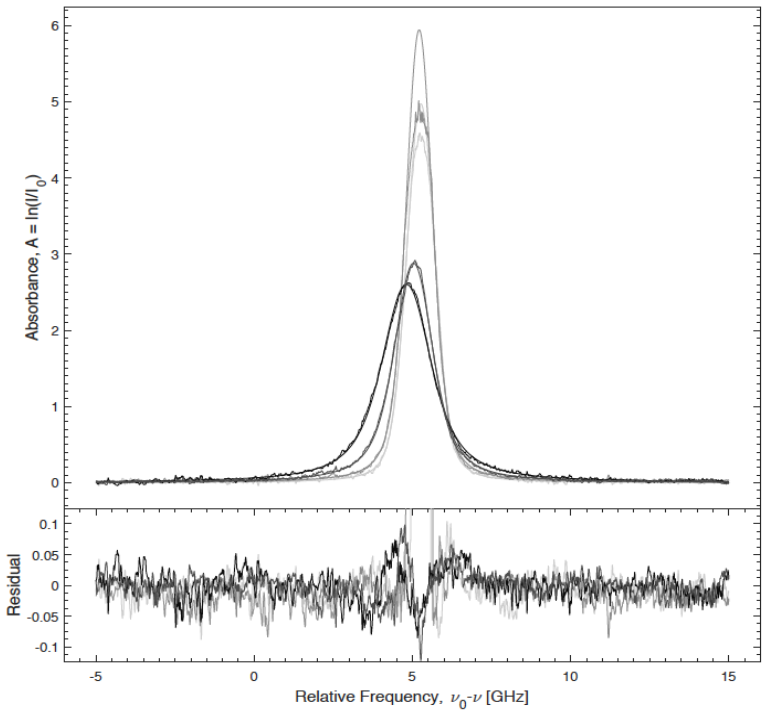

Figure 1. Absorption line shapes without saturation.

Absorption spectra with the high power saturating laser tuned to near line center are shown in Figure 2. The inhomogeneous, 5 Torr spectra are illustrated on the left hand side and the homogenously broadened spectra at 100 Torr on the right. The hole burning effect is clear in the 5 Torr case. For the 100 Torr case, the absorbance is flatter at the top of the line shape. A fit to the saturated line shape function:

$$\begin{aligned} \alpha(\nu) &= \alpha_0(\nu)\frac{\Delta\nu_L/2}{B(1-(\frac{2(\nu-\nu_0)}{A+B})^2)^{1/2}} \\ A &= ((\nu-\nu_0)^2+(\Delta\nu_L)^2)^{1/2} \\ B &= ((\nu-\nu_0)^2+(\Delta\nu_L)^2(1+2S))^{1/2} \end{aligned} \qquad (1)$$

is also illustrated in Figure 2. The degree of saturation, $S= I/I_s$, is influenced by the focused radial spot and the longitudinal bleaching. An assessment of the effective, spatially averaged saturation parameter has been completed and the corresponding fit values from the width of the spectral hole are illustrated in Figure 3.

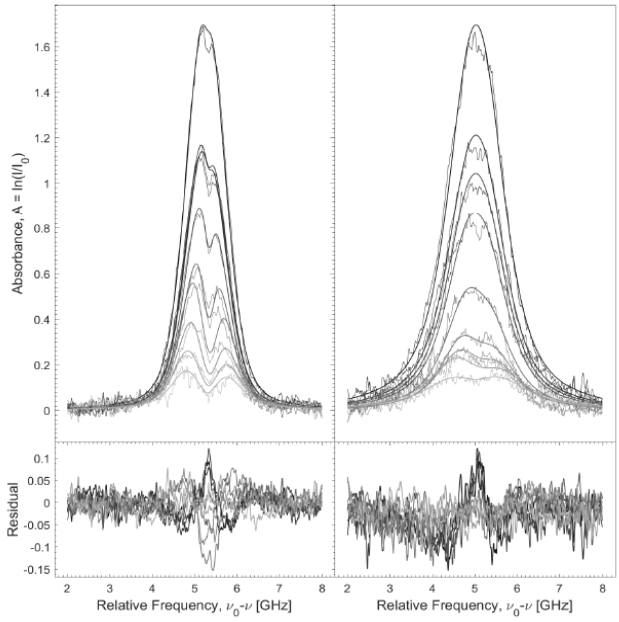

Figure 2. Saturated absorption spectra exhibiting hole burning at 5 Torr (left) and decreased absorption across the full line at 100 Torr (right).

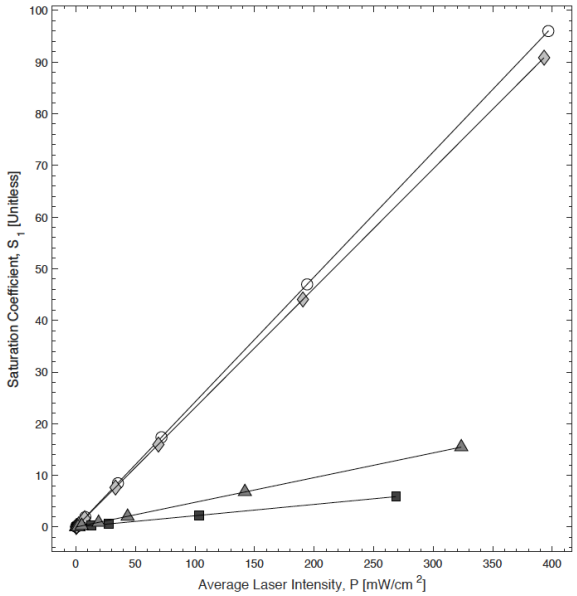

Figure 3. Scaling of saturation parameter with average laser intensity for argon pressures of (o) 5, (◇) 10, (△)50, and (□) 100 Torr.

b. Concentrations of Ar $2p_i$-states

The populations of the excited argon $1s_5$ and $2p_i$ configurations in a 10 W RF discharge was studied using optical emission and diode laser absorption spectroscopy. By optically bleaching the $1s_5 \rightarrow 2p_9$ transition with a narrow band laser pump of about 10 W/cm^2 at 811 nm, the $2p_9$ population was increased by about a factor of 2 at a pressure of 5 Torr. At higher pressure, collisional mixing to adjacent p-states limited the laser-increased $2p_9$ population to less than 10 percent. All other laser-induced p-state populations were minimally affected at low pressure and increased by about a factor of 4 at higher pressure. The $1s_5$ population was greater than 8.2×10^{12} cm^{-3} at a pressure of 5 Torr, and 58 percent of this population was moved to the $2p_9$ state at 828 mW, or about 10 W/cm^2.

c. Micro-Cathode Sustained Discharge Array

The three-electrode microhollow cathode discharge (MCD), also known as the microhollow cathode sustained discharge (MCSD), was first developed by Stark in 1999 and operated at atmospheric pressure in argon and air [1]. The direct-current (DC) MCSD has been used for plasma processing of materials [2] and the pulsed MCSD has been used for Xe excimer emission [3]. The idea of the MCSD is shown in Figure 4. The first radio-frequency (RF) MCSD array (MCSDA) was developed by Barankova in 2000 and has operated at powers of 20 W and discharge volumes as large as 28 cm^3 using neon and argon[4]. These arrays were also used for cold plasma treatment of large substrates [5-6]. There has been a recent modeling effort to analyze these MCDs and MHCDAs [7,8] and development of these discharges has continued for their efficient excimer emission in a pulsed scheme [9-11] and for plasma processing [12-13] but investigations of the excited state production of inert gases inside the large plasma volume is absent.

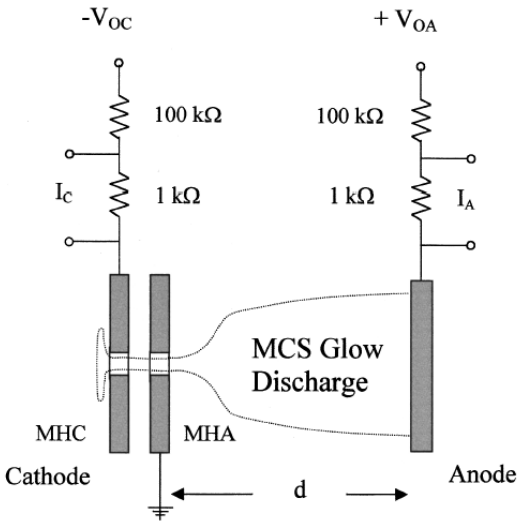

Figure 4. A direct-current MCSD with individual ballast resistors [2].

The discharge operates as follows; Ar/He mixtures flow through the top plate of the discharge which is connected to a 13.56 MHz RF power source. Highly ionized plasma forms inside the microholes. The DC biased plate is then used to draw the high energy electrons out of the holes into the larger volume where they sustain a large-volume atmospheric pressure glow discharge. In the single MCSD case the plasma forms an expanding cone, as seen in Figure 4. In the case of the MCSDA, these cones will overlap and form a semi-homogeneous plasma near the bottom plate. The essence of this configuration is to emulate the influence of a UV-assisted discharge with extraction of high energy electrons formed in the microplasmas instead of low energy electrons removed from the surface of a metal.

The AFIT Micro-Cathode Sustained Discharge Array (MCSDA) is illustrated in Figure 5. The array contained 992, 5 micron holes in a 1 cm x 2 cm three layer structure of 250 μm thick alumina between copper plates. Within the holes, the electric field is high and provides a high density source of energetic electrons. The plasma is extended into a large volume by a third electrode. The spacing of the array and the third plate is 0.5 cm, corresponding to a total volume of 1 cm^3. At 20 W of delivered RF power, a stable, uniform glow was sustained between the array and the third electrode. In the current design, parasitic power losses were suffered in the flow chamber due to unshielded input electrodes. This can be resolved by improving the impedance match between the power supply and plasma, and eliminating the parasitic losses. Further development and characterization of the plasma should lead to excitation volumes of greater than 10 cm^3, primarily by extending the length of the array.

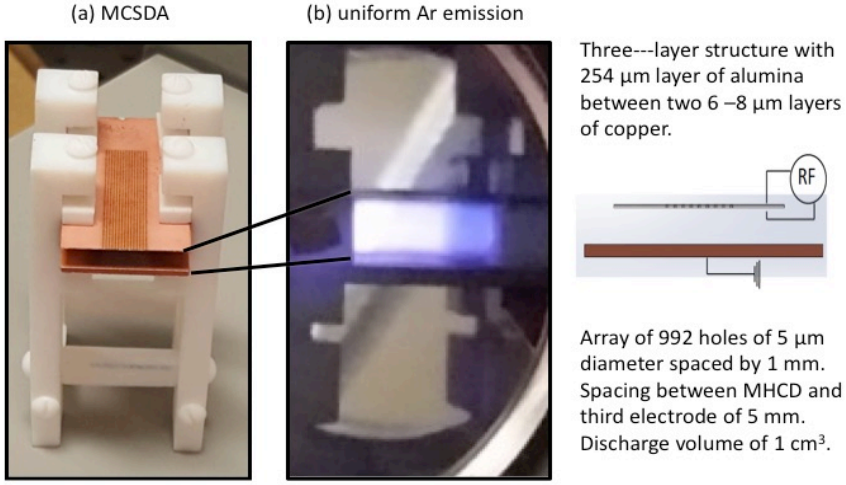

Figure 5. (a) Micro-Cathode Sustained Discharge Array (MCSDA) hardware and (b) image of sustained, large volume fluorescence.

d. RF dielectric barrier discharge.

A second large volume, high pressure argon discharge has been developed using a cylindrical anode/cathode above and below the full glass tube, as shown in Figure 6. The emission was very uniform filling the full 4 mm diameter tube along the length of the electrodes. The power requirement for the discharge was low, ~ 20 W. Studies of the radial distribution of $1s_5$ metastable density and flow instabilities as a function of flow rate were carried out.

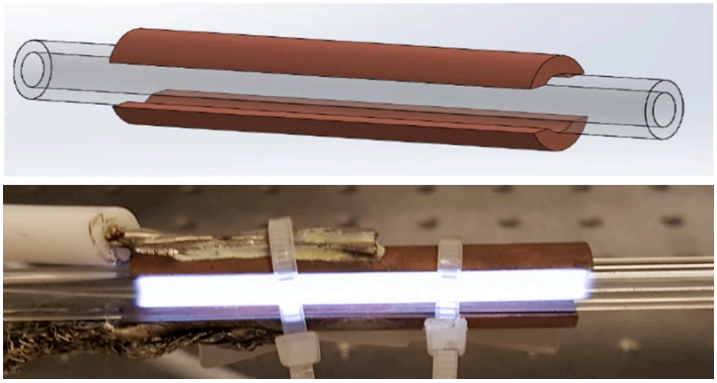

Figure 6. Cylindrical dielectric barrier discharge with RF excitation.

e. Laser and discharge modeling

A five-level laser model has been developed at AFIT to describe the observed population distributions in the high-volume, atmospheric pressure radio-frequency discharges both with and without optical pumping. The five level model involves the kinetics for the levels $1s_5$, $1s_4$, $2p_{10}$, $2p_9$ and $2p_8$ and the mechanisms involved include electron impact production, electron impact spin-orbit mixing, argon collisional spin-orbit mixing, and helium collisional spin-orbit mixing. All the rates are taken from the literature with the electron rates and Ar s to p rates coming from Zhu (14) and Cheng (15) and the argon and helium s to s and p to p rates coming from Han, et al (16-17). The mechanisms included in the model are given in Table 1 with their forward rates. The reverse rates are found using detailed balance. A gas temperature dependence has been added to the rate coefficients to account for the temperature dependence of the mean velocity only, since the dependence of the cross sections is unknown. It is also worth noting that the electron rates were measured in experiments for electron temperatures ranging from one to two orders of magnitude greater than the expected mean electron temperature in these discharges. The authors predict that the rates are likely higher than the trends predict at low electron temperatures. In our model this may lead to an overestimation of the electron density which could be offset by artificially increasing the electron rates.

Table 1. The mechanisms and associated rates are given. Modified rates have the factor by which they were modified in the model included in parenthesis before the literature rate (e.g. (6) 0.4 x 10-11 (Tg/300)0.5 implies 2.4 x 10-11 (Tg/300)0.5). Te is the electron temperature in electron Volts and Tg is the gas temperature in Kelvin.

Mechanism	Rate Coefficient [$cm^3 s^{-1}$]	Mechanism	Rate Coefficient [$cm^3 s^{-1}$]
$e^- + Ar \leftrightarrow Ar^*(s5) + e^-$	2.7×10^{-9} Exp[-11.9/Te]	$Ar + Ar^*(p10) \leftrightarrow Ar^*(s5) + Ar$	$1.5 \times 10^{-11} (Tg/300)^{0.5}$
$e^- + Ar \leftrightarrow Ar^*(s4) + e^-$	3.5×10^{-9} Exp[-12.3/Te]	$Ar + Ar^*(p9) \leftrightarrow Ar^*(s5) + Ar$	$3 \times 10^{-11} (Tg/300)^{0.5}$
$e^- + Ar \leftrightarrow Ar^*(p10) + e^-$	2×10^{-9} Exp[-13.0/Te]	$Ar + Ar^*(p8) \leftrightarrow Ar^*(s5) + Ar$	$4 \times 10^{-11} (Tg/300)^{0.5}$
$e^- + Ar \leftrightarrow Ar^*(p9) + e^-$	1.9×10^{-9} Exp[-13.5/Te]	$Ar + Ar^*(p10) \leftrightarrow Ar^*(s4) + Ar$	$1.5 \times 10^{-11} (Tg/300)^{0.5}$
$e^- + Ar \leftrightarrow Ar^*(p8) + e^-$	2.2×10^{-9} Exp[-13.6/Te]	$Ar + Ar^*(p9) \leftrightarrow Ar^*(s4) + Ar$	$3 \times 10^{-11} (Tg/300)^{0.5}$
$e^- + Ar^* (s5) \leftrightarrow Ar^*(s4) + e^-$	$1 \times 10^{-7} Te^{-0.6}$	$Ar + Ar^*(p8) \leftrightarrow Ar^*(s4) + Ar$	$4 \times 10^{-11} (Tg/300)^{0.5}$
$e^- + Ar^*(s5) \leftrightarrow Ar^*(p10) + e^-$	(1/2) 1.9×10^{-7} Exp[-1.69/Te]	$Ar + Ar^*(p9) \leftrightarrow Ar^*(p10) + Ar$	$2.6 \times 10^{-11} (Tg/300)^{0.5}$
$e^- + Ar^*(s5) \leftrightarrow Ar^*(p9) + e^-$	1.5×10^{-7} Exp[-2/Te]	$Ar + Ar^*(p8) \leftrightarrow Ar^*(p9) + Ar$	$1.1 \times 10^{-11} (Tg/300)^{0.5}$
$e^- + Ar^*(s5) \leftrightarrow Ar^*(p8) + e^-$	8.6×10^{-8} Exp[-1.85/Te]	$Ar + Ar^*(p8) \leftrightarrow Ar^*(p10) + Ar$	$1.1 \times 10^{-11} (Tg/300)^{0.5}$
$e^- + Ar^*(s4) \leftrightarrow Ar^*(p10) + e^-$	8.6×10^{-8} Exp[-1.73/Te]	$He+ Ar^*(s5) \leftrightarrow Ar^*(s4) + He$	$1 \times 10^{-13} (Tg/300)^{0.5}$
$e^- + Ar^*(s4) \leftrightarrow Ar^*(p8) + e^-$	1×10^{-7} Exp[-2/Te]	$He+ Ar^*(p9) \leftrightarrow Ar^*(p10) + He$	(3) $1.6 \times 10^{-11} (Tg/300)^{0.5}$
$e^- + Ar^*(p10) \leftrightarrow Ar^*(p9) + e^-$	$4 \times 10^{-7} Te^{-0.6}$	$He+ Ar^*(p8) \leftrightarrow Ar^*(p9) + He$	$4.5 \times 10^{-11} (Tg/300)^{0.5}$
$e^- + Ar^*(p10) \leftrightarrow Ar^*(p8) + e^-$	$4 \times 10^{-7} Te^{-0.6}$	$He+ Ar^*(p8) \leftrightarrow Ar^*(p10) + He$	(6) $0.4 \times 10^{-11} (Tg/300)^{0.5}$
$e^- + Ar^*(p9) \leftrightarrow Ar^*(p8) + e^-$	$4 \times 10^{-7} Te^{-0.6}$		

The model is parameterized by three terms: the electron temperature, the electron number density and the gas temperature. Since the medium in question is a plasma at high pressure, the gas temperature is near impossible to extract directly from the Doppler Width of a Voigt Fit. Similarly, since the electron density is sufficiently low relative to the gas pressure the stark broadening is not a significant contributor to the line shape and so the number density of electrons cannot be extracted from the data. Finally, the general method for approximating Te comes from considering line ratios between transitions of Ar^+ and Ar*. The Ar^+ energy levels are significantly higher than ionization and so the Ar+ excited state population densities are expected to be very low. This is consistent with the fact that there are no ion lines visible in the spectrum. These three parameters become our tuning knobs for the model. These knobs are tuned until the model output matches measured number densities and population ratios. That is, the model matches the $1s_5$ and $1s_4$ number densities as measured in a tunable diode laser absorption spectroscopy (TDLAS) experiment as well as the population ratios of $2p_9/2p_{10}$, $2p_8/2p_9$ and $2p_8/2p_{10}$ as measured from the discharge fluorescence both with and without optical pumping. The model is then extended to match PSI's published gain and absorbance measurements for the $1s_5$-$2p_{10}$ transition.

The electron temperature, electron density and gas temperature are expected to change with pressure from physical arguments. Specifically, the electron temperature is expected to decrease with increasing pressure since the E/N will decrease with fixed RF input power. The electron density is expected to increase since the number of ionizing collisions will increase with Ar density. Finally, the gas temperature will either increase or decrease depending on the heat transfer kinetics, the larger heat capacity at increased pressure, the increased mass flow through the discharge, and the greater thermalization of electrons in the plasma.

An initial examination of the model leads to the conclusions that the electron temperature essentially drives the magnitude of the populations in the excited states whereas the gas temperature and electron density are the determiners of the population ratios. It is with this knowledge that we proceed in trying to fit the data using the model. First, we discuss how the data was obtained.

The first parameter that needs to be set in the model is the electron temperature. It is observed that the main influence of the electron temperature is to change the magnitude of the populations. Its influence on the ratios is minimal. In Figure 7 we show the model predicted values of the sum of the $1s_4$ and $1s_5$ number densities. The intersection between those curves and the measured number densities provides a small range of electron temperatures for which the model matches the data.

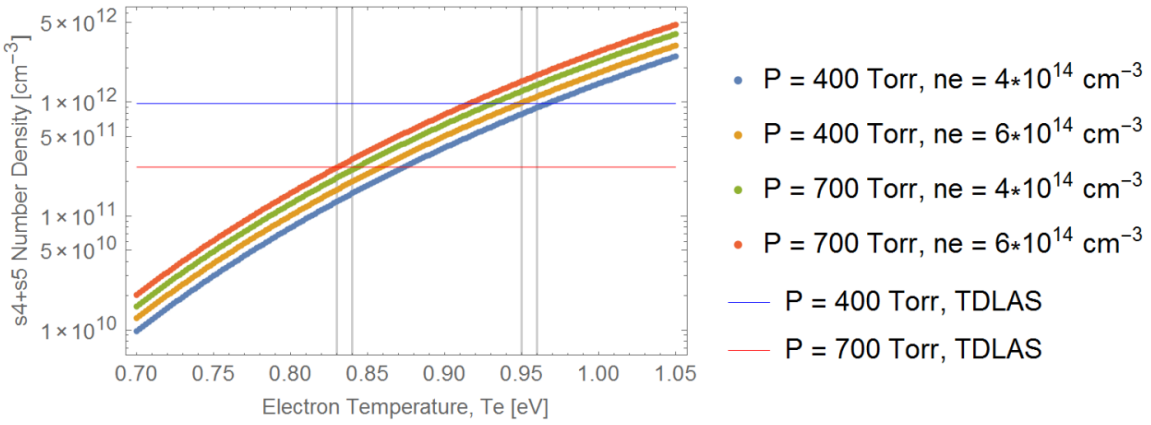

Figure 7. The model output for the $1s_4$+$1s_5$ number density as a function of the electron temperature is shown. It is compared to the measured number densities at two pressures, 400 and 700 Torr. The vertical lines show the intersection points between the model prediction and the measured densities. The electron temperature is seen to fall into a small range dependent on the electron density and to decrease with pressure.

We see that for the 400 Torr case the electron temperature can be between 0.95 and 0.96 eV if the electron density is as presented and it falls to between 0.83 and 0.84 eV for the 700 Torr case. This is driven by the decreasing number density at 700 Torr although even if the number density did not decrease the electron temperature would still have to decrease but by a much smaller amount. Furthermore, increasing the electron density will shift these curves to higher predicted $1s_4$+$1s_5$ number density in a linear fashion and so the electron number density chosen later will influence these curves, although not substantially.

The population ratios of the p states offer another temperature diagnostic in the discharge. By examining the model prediction of the population ratios as a function of gas temperature and comparing them to the measured ratios we can get an idea of what the gas temperature should be.

In Figure 8 we see that the population ratio between the $2p_{10}/2p_9$, $2p_{10}/2p_8$ and $2p_9/2p_8$ states for various pressures gives a fairly wide range of gas temperatures from 750 to 1000 K. The model predicts that there is no significant temperature dependence as a function of pressure for these population ratios.

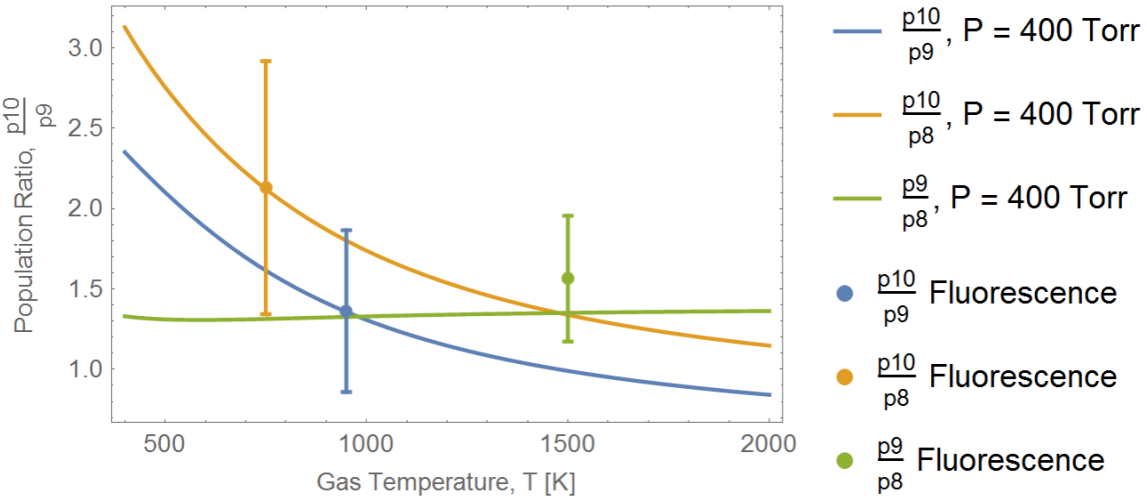

Figure 8. The model prediction, solid lines, for the population ratios as a function of temperature is shown. It is compared to the measured population ratios at a pressure of 400 Torr. The gas temperature ranges from 750 to 1000 K for the $2p_{10}$ ratios and does not match the $2p_9/2p_8$ ratio well, although the whole curve is within the error of the ratio.

The final piece of data to which the model fits is the PSI gain and absorbance curves.[18] For these measurements the electron temperature is used to give an approximate number density (on the order of 5×10^{12} cm^{-3}). The electron density is then used to fit the absorbance measurement made with a 7 W/cm^2 probe laser and the gain at 4 kW/cm^2 of optical pumping. This can be seen in Figure 9.

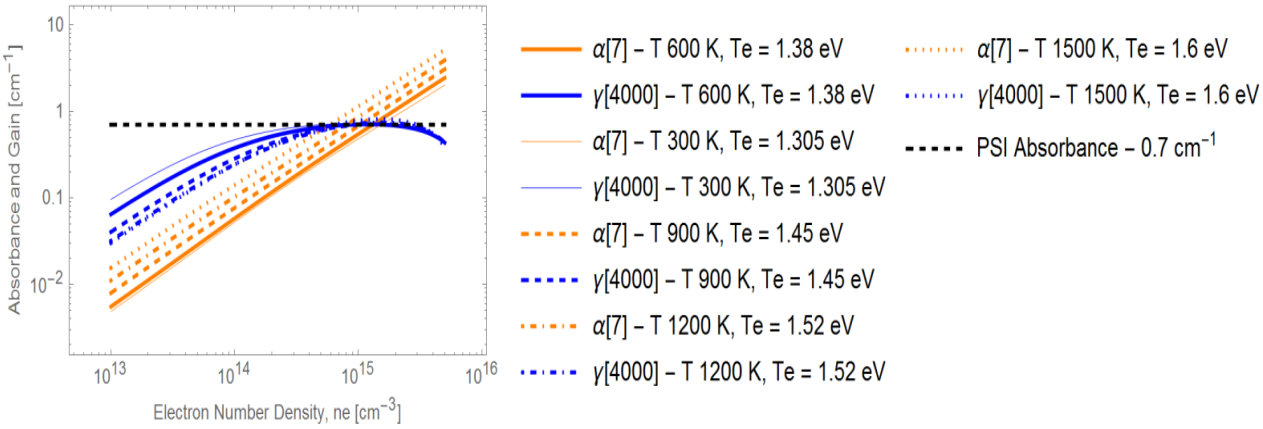

Figure 9. The absorbance and gain are plotted as a function of the electron density for various combinations of gas temperature and electron temperature combinations. Each gas temperature, electron temperature pair have an associated number density at which the model prediction will match the measurements.

The five-level laser model sufficiently captures the kinetics of the large-volume, atmospheric pressure RF discharge in the absence of a pump laser and manages to capture the gain and absorbance trends measured by PSI in the micro discharge case. The model uses rates from the literature and is parameterized by electron density, electron temperature and gas temperature.

References for section 3

[1] R. H. Stark and K. H. Schoenbach, Appl. Phys. Let. **85,** 2075 (1999).
[2] H. Park, T. Lee, K. W. Park, H. K. Baik, S. Lee, and K. M. Song, Appl. Phys. Let. **82,** 3191 (2003).
[3] M. Moselhy, W. Shi, R. H. Stark, K. H. Schoenbach, Appl. Phys. Let. **79**, 1240 (2001).
[4] H. Barankova, and L. Bardos, Appl. Phys. Let. **76**, 285 (2000).
[5] Y. Guo, F. C. Hong, Appl. Phys. Let. **82**, 337 (2003).
[6] H. Barankova, and L. Bardos, Surface and Coatings Technology, 163-164 (2003).
[7] J. P. Beouf, L. C. Pitchford, and K. H. Schoenbach, Appl. Phys. Let. **86**, 071501 (2005).
[8] A. Berkane, S. Rebial, F. Bouanaka, and H. Bahouh, Phys. Scr. **90** (2015).
[9] M. Moselhy, I. Petzenhauser, K. Frank, and K. H. Schoenbach, J. Phys. D: Appl. Phys. **36** (2003).
[10] B. J. Lee, H. Rahaman, S. H. Nam, K. P. Giapis, M. Iberler, J. Jacoby, and K. Frank, Physics of Plasmas **18**, 083506 (2011).
[11] B. J. Lee, H. Rahaman, S. H. Nam, M. Iberler, J. Jacoby, and K. Frank, Physics of Plasmas **20**, 123510 (2013).
[12] J. S. Sousa, G. Bauville, and V. Puech, Plasma Sources Sci. Technol. **22** (2013).
[13] H. Barankova, and L. Bardos, Vacuum **87** (2013).

[14] Zhu, Xi-Min and Pu, Yi-Kang. J. Phys D: Appl Phys. 43, 015204 (2010)
[15] Cheng, Zhi-Wen, et al, J. Phys. D: Appl Phys 47, 275203 (2014)
[16] Han, J and Heaven, M C. Optics Letters. 39, 22 (2014).
[17] Han, Jiande, et al, Optics Letters. 38, 24 (2013).
[18] Rawlins, W. T., et al, Proc. Of SPIE 8962, 896203-1 (2014).